# PARASITIC PRODUCTION OF COBALT-57 FOR QUALITY CONTROL USE

by
ALEXANDER JAMES NEALE

A thesis submitted to the University of Birmingham for the degree of MASTERS BY RESEARCH (MRes).

School of Physics and Astronomy
Medical Physics
University of Birmingham
September 2019

## Abstract

Routine quality control is performed in all nuclear medicine departments and requires image uniformity measurements of gamma camera systems. Cobalt-57 ($^{57}$Co) flood sources are well suited to this task due the energy emissions of $^{57}$Co being similar to the main nuclear medicine radionuclide of Technetium-99m ($^{99m}$Tc). One method for producing $^{57}$Co is proton bombardment of nickel.

An equally important isotope is Rubidium-81 ($^{81}$Rb) which decays to Krypton-81m ($^{81m}$Kr) and used in the diagnosis of pulmonary embolism. Rubidium-81 is produced by proton bombardment of enriched $^{82}$Kr gas contained in a nickel plated target.

Presented in this work is a detailed investigation of cyclotron production conditions whereby both $^{81}$Rb and $^{57}$Co yields are at maximum and produced simultaneously. Production in this manner is seen by the author as novel and desirable as overall costs for producing both isotopes is reduced.

A number of nuclear reactions were investigated theoretically which were then tested experimentally. A comprehensive review of known data bases gave published reaction data. These data were used to make predictions around target yield and more importantly contaminant isotope yields.

A way to utilise the parasitically produced $^{57}$Co for production of radioactive quality control sources was also investigated. This showed the concept of thermal drop on demand printing of a flood source to give high uniformity required for flood source manufacture.

## Acknowledgments

I would to thank my project supervisor, Professor David Parker for his continued help throughout the entire project, and who went above and beyond his role on more than one occasion. I would also like to thank Dr. Bill Thomson and Dr. Alp Notghi for supporting this project.

# Parasitic Production of Cobalt-57 for Quality Control Use

## Contents

**Chapter 1:** Background to the Area of Study ..... 3
1.1 Introduction to Area of Study ..... 3
1.2 Rubidium-81 ..... 3
1.3 Cobalt-57 ..... 5
1.4 Isotope Production ..... 6
1.5 Cyclotrons ..... 8
1.6 Scanditronix MC40 ..... 10
1.7 Interaction of Charged Particles with Matter ..... 12
1.8 Nuclear Reaction Barriers ..... 13
1.9 Types of Nuclear Reactions ..... 15
1.10 Nuclear Reaction Cross Section Data ..... 16
**Chapter 2:** Theory of Simultaneous Dual Isotope Production ..... 17
2.1 Examination of Relevant Proton Kinetics and Reactions ..... 20
**Chapter 3:** Experimental Testing Of Simultaneous Dual Isotope Production ..... 26
3.1 Calibration of High Purity Germanium Detector ..... 27
3.2 Results from Analysis of Irradiated Discs ..... 29
3.3 Discussion of Experimental Results ..... 30
3.4 Predictions of Optimum Target Thickness and Energy ..... 31
**Chapter 4:** Further Work to Utilise Simultaneous Dual Isotope Production ..... 36
4.1 Chemical Processing of the Target ..... 36
4.2 Uniform Flood Source Production via Thermal Drop On Demand Printing ..... 37
**Chapter 5:** Discussion of Findings ..... 41
5.1 Evaluating Cross Section Data ..... 41
5.2 Computerized Calculation of Product Yields for Multiple Conditions ..... 42
5.3 Discussion of Experimental Results ..... 43
5.4 Discussion of Live Rubidium / Cobalt Production ..... 44
5.5 Predictions about Target Thickness and Composition ..... 45
5.6 Production of Radioactive Flood Sources ..... 46
**Chapter 6:** Conclusion ..... 47

Works Cited:.....48
Appendix 1: Calculations of Radioactive Yield.....50
Appendix 2: Printed Flood Source Data.....52
Appendix 3: Composite Flood Source Image.....54


UNIVERSITY OF BIRMINGHAM

# Chapter 1: Background to the Area of Study

## 1.1 Introduction to Area of Study

The field of nuclear medicine is based on the use of radioisotopes and without them could not exist. Typically a radioisotope will be processed into a radiopharmaceutical and administered to a patient. The radioactive emission of the isotope will then have a net benefit to the patient by means of a therapeutic effect or providing diagnostic information about the patient when imaged with a gamma camera or PET scanner. Therefore the supply and availability of radioisotopes is particularly important to this international discipline of medicine.

This project focuses on two important isotopes and a novel production method which allows both to be produced from the same proton bombardment. This method will be especially important whenever economic factors play a part in access to radioisotopes.

The aim of this project is to develop a method for producing $^{81}$Rb and $^{57}$Co simultaneously and utilising both isotopes for separate final products. A description of the isotopes and usage are as follows:

## 1.2 Rubidium-81

Rubidium-81 is useful to the nuclear medicine community due to its daughter nucleus $^{81m}$Kr. The physical characteristics of both parent and daughter nuclei lend them to a generator type product. These isotope 'generators' are common where the desired daughter nucleus has an unworkably short half-life; whereas the parent nuclide half-life is long enough to allow for manufacture and transport to the point of use. In these instances the parent isotope is often prepared into a unit or generator that allows for the separation of the daughter nucleus, a process often referred to as an elution (Powsner, 2008). The physical properties of these isotopes are shown in Table 1.

| Isotope | Half Life ($T_{1/2}$) | Notable energy emission | Elemental State |
|---|---|---|---|
| **$^{81}$Rb (Parent)** | 4.57 *hours* | 431 keV | Solid alkali metal |
| **$^{81m}$Kr(Daughter)** | 13 *seconds* | 190.6 keV | Gas |

*(Table 1: Physical Properties of Rubidium / Krypton Isotopes, (Brookhaven-National-Laboratory, 2016).*

The physical properties of $^{81m}$Kr are advantageous for a number of reasons.

Krypton-81m decays via an isomeric transition emitting a single 191 keV gamma ray so there are no radiation emissions that would unnecessarily increase the radiation dose to the patient, such as a charged particle or multiple high energy gamma rays. Alpha and beta radiation is undesirable for diagnostic imaging as this type of radiation cannot be imaged with a conventional single photon gamma camera. Such decays also carry a higher radiation burden to the patient due to the greater levels of ionization within the tissues of the human body. The short half-life of 13 seconds also contributes to a lower radiation dose from this isotope, as the patient is not exposed to radioactive decay long after the imaging procedure has ended.

Gamma-ray photons with energies below the MeV range interact with matter by either photoelectric absorption or Compton scattering, and the relative probabilities depend on the photon energy and the Z number of the material. The majority of the isotopes used in nuclear medicine imaging have gamma energies in the 100 to 200 keV range. Gamma cameras are therefore optimised for this energy range, being thinner sodium iodide (NaI) crystals as opposed to thicker crystals. A thinner NaI crystal will give the imaging system improved spatial resolution due to the light captured from the interaction of the gamma ray with the crystal being closer to the source of the original interaction. A thinner NaI crystal however is less sensitive as there is less of the crystal to stop the gamma ray. This is where the type of interaction which the gamma ray undergoes becomes more important. If the gamma ray has a higher energy it will be more likely to undergo Compton scattering, which will deliver less energy to the crystal as the photon may not be fully absorbed. Also the scintillation within the crystal will reflect the photon's scattered trajectory as opposed to its true origin. The combination of a lower gamma energy such as 191 keV and the high Z number of NaI means the predominant type of interaction will be photo electric absorption. This makes the photon much more likely to be fully absorbed within a thinner NaI crystal giving more accurate spatial information (Powsner, 2008).

The elemental state of $^{81m}$Kr lends itself for use as a ventilation imaging agent as the inert gas mixes homogenously with humidified air. As the physical state of the parent isotope is solid, $^{81m}$Kr can be eluted from the generator system by passing air over a suitable medium that will retain the $^{81}$Rb but release the $^{81m}$Kr gas.

The eluted $^{81m}$Kr gas is then used as a ventilation agent in the diagnosis of pulmonary embolism (P.E.). The patient will typically inhale the gas continually during the imaging procedure. The provision of ventilation / perfusion (V/Q) imaging is

important to the National Health Service and is often required 5 days per week. Pulmonary embolism is a serious condition where a deep vein embolus travels to the heart via venous circulation, where it will enter the lungs after passing through the right side of the heart. As soon as the embolus reaches the capillary bed it becomes lodged in the narrow vessels. This occludes the vessel from supplying the alveoli with haemoglobin rich blood which would normally return via the heart to oxygenate the rest of the body. This occlusion or embolism can be detected on a nuclear medicine V/Q scan by the absence of blood supply in an area of the lung that shows evidence of ventilation. A radioactive macroscopic tracer is injected into the blood stream which also will not pass through the capillary bed owing to the size of the particles. In turn this tracer will not be able to pass an occluded portion of the lung or the capillary bed beyond the embolism, hence creating a mismatch between the perfusion and ventilation (see Figure 1).

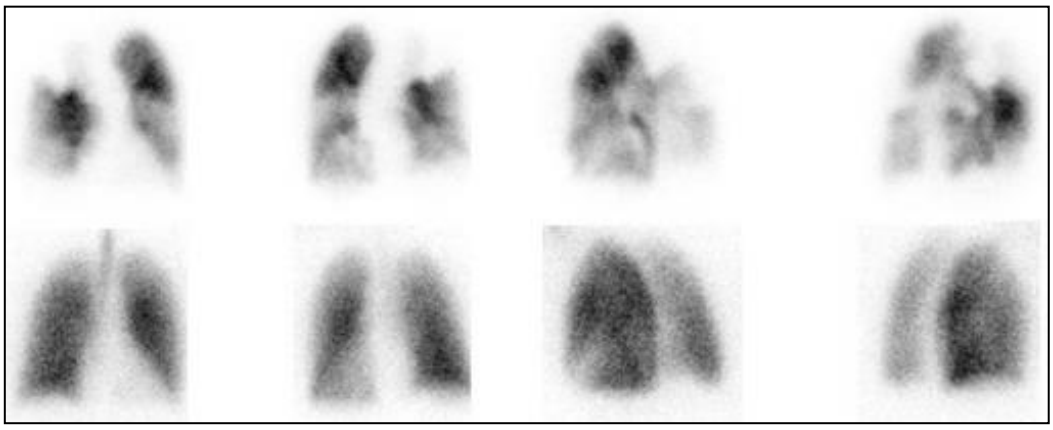

*(Figure 1: (Top: L-R)Anterior, Posterior, Left Posterior Oblique, Right Posterior Oblique, Perfusion Images with $^{99m}$Tc, Showing Multiple Defects.(Bottom: L-R) Anterior, Posterior, Left Posterior Oblique, Right Posterior Oblique, Showing Normal Ventilation with $^{81m}$Kr Gas).*

### 1.3 Cobalt-57

Quality assurance (QA) is vital to the work done in nuclear medicine, particularly gamma camera QA. The most common daily QA task is to check the uniformity of the gamma camera detector. This is usually performed with a known high uniformity $^{57}$Co 'flood source'. The principle is to flood the detector with a uniform field of radiation. Therefore, the resulting image should also be highly uniform. A non-uniformly responding detector could easily misrepresent the distribution of radioactivity within the patient, potentially causing an incorrect diagnosis. Using the perfusion images shown in Figure 1, imagine that the areas of the lung which do not show localisation of the radio-tracer (photopenic areas) were in fact caused by non-

uniform detector response instead of pulmonary emboli. Cobalt-57 is well suited to this essential quality test possessing a reasonable half-life giving flood sources a 1 to 3 year working life. The isotope's physical properties are shown in Table 2.

| Isotope | Half Life ($T^{1/2}$) | Notable energy emission | Elemental State |
|---|---|---|---|
| **$^{57}$Co** | 271.8 days | 121 keV | Transition metal |
| **$^{99m}$Tc** | 0.25 days | 140 keV | Transition metal |

*(Table 2: Physical Properties of Radionuclides (Brookhaven-National-Laboratory, 2016).*

The most widely used isotope in nuclear medicine is $^{99m}$Tc, with its single gamma ray emission of 140 keV (Sorenson, 2012). This isotope however has a short half-life of 6.02 hours which is ideal for patient administration but impractical for use in a daily uniform QC flood source. It is important to check the uniformity of the gamma camera's response across the imaging field of view as non-uniformities will affect the diagnostic images of the patient. The uniformity is based on an energy correction map for 140 keV, so naturally an isotope of the same energy would be best to check this map on a daily basis. As mentioned this isotope would need to have a reasonably long half-life as creating a high uniformity source can be labour intensive. In this instance $^{57}$Co has the desirable properties of similar gamma-ray energy to $^{99m}$Tc yet has a much longer half-life.

### 1.4 Isotope Production

Radioisotopes exist because the nucleus of an atom has become unstable either by excessive energy or due to an imbalance between the protons and neutrons. A nucleon imbalance can either be in favour of the protons or neutrons and this therefore dictates the properties of the atom. Figure 2 shows a chart of nuclides and their properties (if accessed electronically).

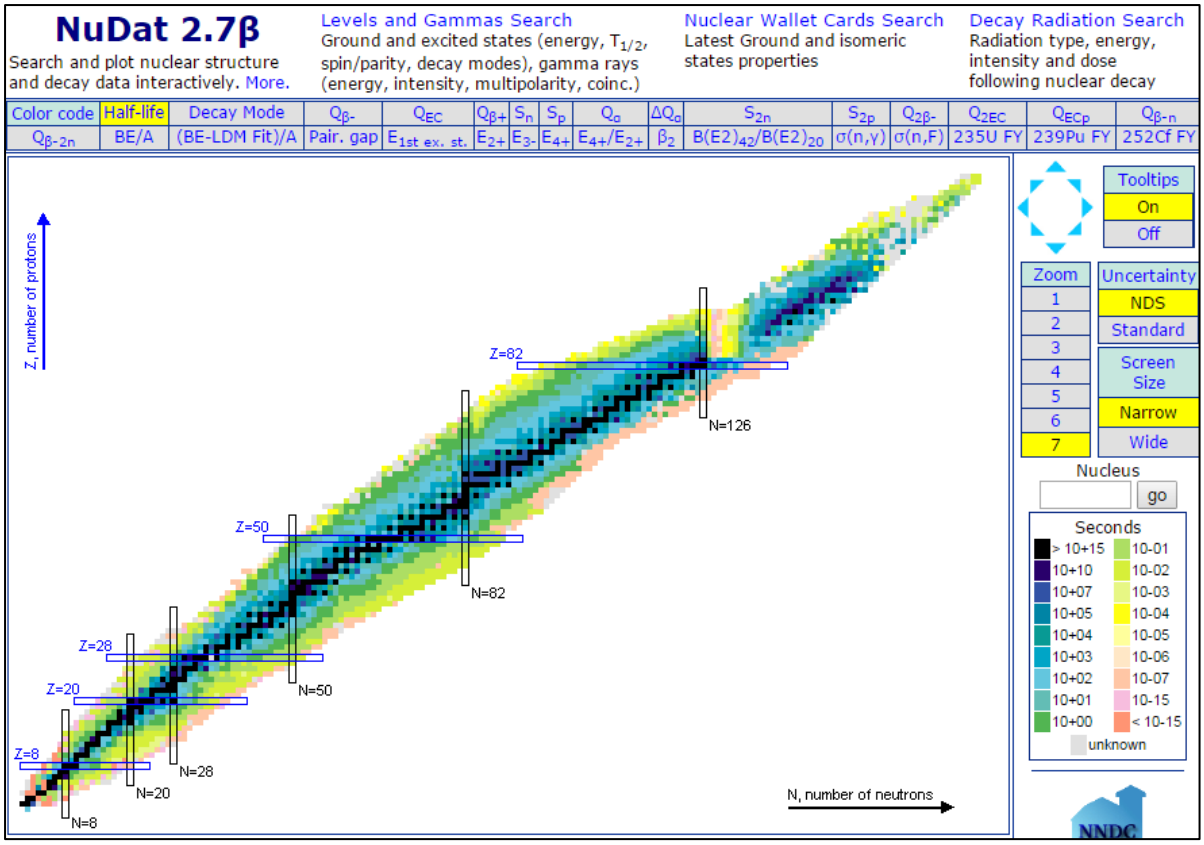


*(Figure 2: Chart of Nuclides (Brookhaven-National-Laboratory, 2016).*

In the field of modern nuclear medicine the only valuable radionuclides are created artificially by altering the combination of nucleons within the atom (Sorenson, 2012). The production method of these is generally dictated by the requirement of the desired atom being either neutron or proton rich in order to gain the desired physical properties.

Two primary methods for producing medical radioisotopes are particle accelerator and nuclear reactor production. A charged particle accelerator will generally produce proton rich atoms. For example if protons are accelerated to high energies and then strike a target nucleus a common *(p,n)* reaction may take place. In this reaction the target nucleus captures the proton and ejects a neutron.

Nuclear reactor production can cause the inverse of this reaction (although it is rare), whereby neutrons released from nuclear fission strike a target nucleus and are captured, (*n,p*), resulting in the loss of a proton from the atom. This process is an example of fast neutron activation (Sorenson, 2012). However, it is a thermal neutron flux that more commonly will cause a nuclear reaction as the lower velocity of these neutrons make them much more likely to interact with a target nucleus. Thermal neutrons typically cause emission of a gamma ray from the target nucleus

(*n,γ)* once captured. A relevant example of this reaction is the production of Molybdenum-99 ($^{99}$Mo), the parent isotope of $^{99m}$Tc (IAEA, Manual for reactor produced radioisotopes, 2003):

$^{98}Mo + n \rightarrow {}^{99}Mo + \gamma$

Of the two primary isotope production methods, accelerator based production is generally much more accessible to the medical community. Accelerators usually require much less financial investment than reactors, although still comparatively high compared to mainstream pharmaceutical production. Particle accelerators are also free of the added safety and usage concerns that reactors pose, due to the lack of fissile material. This project therefore focuses on radioisotopes produced via a cyclotron.

### 1.5 Cyclotrons

A cyclotron is a type of particle accelerator capable of driving charged particles in a circular path. This allows the same accelerating structure to be used a number of times, so higher particle energies can be reached compared with linear accelerators for a given length of accelerating element (Wille, 2000).

Particles are introduced into the centre of the accelerating structure by an ion source (see 'S' in Figure 3); a device that uses a high voltage arc in a gas to produce ions. In a classic cyclotron the accelerating structure is comprised of two large hollow cavities often referred to as "dees" given their shape (Sorenson, 2012). A radiofrequency voltage is applied between the dees at a selected frequency so the circulating particles always encounter an accelerating electric field. This is possible due to the physical laws that govern the force on a charged particle in a magnetic field, known as the Lorentz force which is given by:

(Equation 1):

$$\vec{F} = e(\vec{v} \times \vec{B} + \vec{E})$$

where

*F* is the force:
*e* is particle energy,
*v* is velocity,
*B* is magnetic flux density,
*E* is electric field.

In order to create this magnetic field a powerful electromagnet encompasses the accelerating dees. The magnetic field does not contribute to the energy gain of a particle but is essential for bending, steering and focusing the charged particle beam. These magnetic fields exert a force perpendicular to the path of a particle which is also known from the Lorentz force law and responsible for the circular orbit of the particles.

The energy for acceleration of the particles comes from the electric field where the electrical potential across the dee gap is changed at precisely the right moment to cause a gain in velocity (energy). The frequency of this potential voltage change is called the cyclotron frequency, which is given by:

(Equation 2):

$$\omega_z = \frac{e}{m} B_z$$

where

$\omega_z$ is the frequency,

$e$ is energy,

$m$ is mass,

$B_z$ is the magnetic field.

The gain in velocity is exactly offset against the gain in radius, so the cyclotron frequency is independent of energy. This is only true however at particle velocities sufficiently below the speed of light that the particle does not gain mass in relation to its energy (Heikkinen, 1992). High vacuum conditions are created within the accelerating structure and beam line to avoid any contaminating particles that may reduce the particle beam intensity and cause unwanted un-stable nuclei (Wille, 2000).

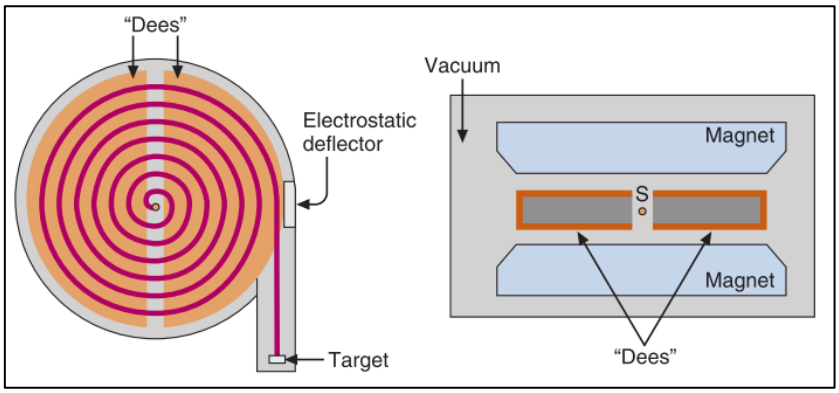


*(Figure 3: Schematic Diagram of a Cyclotron (Sorenson, 2012)).*

Particles are extracted from the cyclotron using a deflector, or in the case of a negative ion accelerator, a stripping foil is used. The particle beam may then be shaped and directed by further magnetic fields or 'steering magnets'. After leaving the cyclotron, accelerated particles will have high levels of kinetic energy typically in the MeV range, which is useful for causing nuclear reactions.

### 1.6 Scanditronix MC40

The University of Birmingham owns and operates a Scanditronix MC40 cyclotron which has been used for the duration of this project. Noteworthy features of the MC40 are that it has two diametrically opposed dees and two dummy dees. The dummy dees are at ground potential and the charged dees can be configured in different accelerating patterns. This gives an advantage over a simpler cyclotron design as 4 accelerating gaps are seen by the particle instead of 2. This also gives the accelerator the flexibility to accelerate a range of positively charged particles at a wide range of energies. These dees or more descriptively 'half dees' are shown in Figure 4.

*(Figure 4: MC40 Dees within the Cyclotron (Nuclear Physics Research Group, 2012)).*

Another desirable feature of the MC40 is its ability to accelerate protons up to 38 MeV. However at this energy a proton will have gained mass as its speed has become relativistic or closer to the speed of light. As described earlier this would cause the proton to drop out of phase with the cyclotron frequency in a classic cyclotron. The MC40 is a type of isocyclotron which overcomes this problem by increasing the static magnetic field towards the outer edges of the cyclotron, thus keeping the particles in phase with the cyclotron frequency. Employing this radially increasing magnetic field has the unwanted effect of spreading the beam out in the vertical plane. To re-focus the beam a system of magnetic field 'hills and valleys' are

used which re-focus the beam. The MC40 has 3 hills and valleys that are twisted in a spiral to gain additional edge focusing (see Figure 5).


*(Figure 5: Magnet Face Showing Spiral Hill / Valleys and Additional Beam Focusing Magnets (Nuclear Physics Research Group, 2012)).*

Important parameters to know when using a cyclotron for radioisotope production are regarding the particle beam output. Flux describes the instantaneous rate of particles passing through an area, whereas fluence is the total charge delivered. Flux is calculated simply by:

(Equation 3):

$$\phi = \frac{I}{e\mathrm{A}}$$

where

$\phi$ flux is equal to;
$I$ is beam current,
$e$ is energy,
A is area.

As the beam from a cyclotron is directed onto a target material, the particles leave the high vacuum conditions of the cyclotron and beam line and encounter matter. What follows is discussed in the following section.

### 1.7 Interaction of Charged Particles with Matter

Given the scale of distance between atomic particles, interactions between particles and a nucleus are relatively uncommon. Broadly speaking, a charged particle spends most of its time interacting with outer atomic electrons, continually losing small amount of energy. Less commonly it is possible for a particle to undergo 'Rutherford Scattering' whereby the path of the particle is altered by a large angle and particle energy is lost.

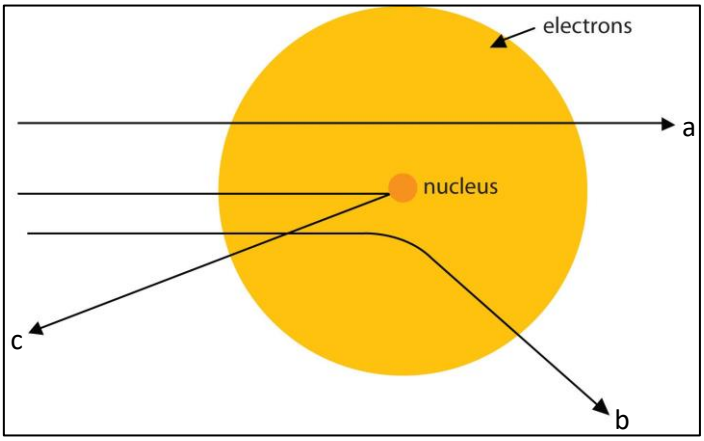


*(Figure 6: Possible Interactions with Matter. a: Predominant Interaction with Orbital Electrons; a, b + c: Rutherford Scattering or Elastic / Inelastic Scattering).*

When orbital electrons are struck by a charged particle they are likely to be scattered causing ionization to the host atom. This random process continually reduces a particle's kinetic energy, and is often referred to as the 'stopping power of the material' which can be quite well defined (Balashov, 1996). This stopping power is a rate of energy loss by the distance travelled and is described mathematically as:

(Equation 4):

$$-dE/dx$$

where

*dE* is the differential loss in energy,

*dx* is the differential distance travelled by the particle.

Here the change in energy is (ΔE) divided by unit distance travelled ($\Delta x$) and can be expressed in units of MeV/mm. Factors affecting $-dE/dx$ include:

- The material density (ρ)
- Initial energy and type of particle.

The mean energy loss of a charged particle after passing through matter is important when calculating the probability that the particle will cause a nuclear reaction. As will be described in later sections, this probability is energy dependent and so will change over the particle's range in matter. A formula for stopping range is given by the Bethe-Bloch formula which, when taking into account relativistic effects can predict the energy loss of fast moving charged particles in matter (Balashov, 1996).

For the purposes of this project it was practical to calculate the stopping range of the protons in matter using an accepted computer program, SRIM (Andersen and Ziegler, 1977). The program produces useful 'look up' tables of stopping power at discrete energies. Figure 7 shows SRIM output for calculated stopping power of $^{nat}$Ni at proton energies of interest.

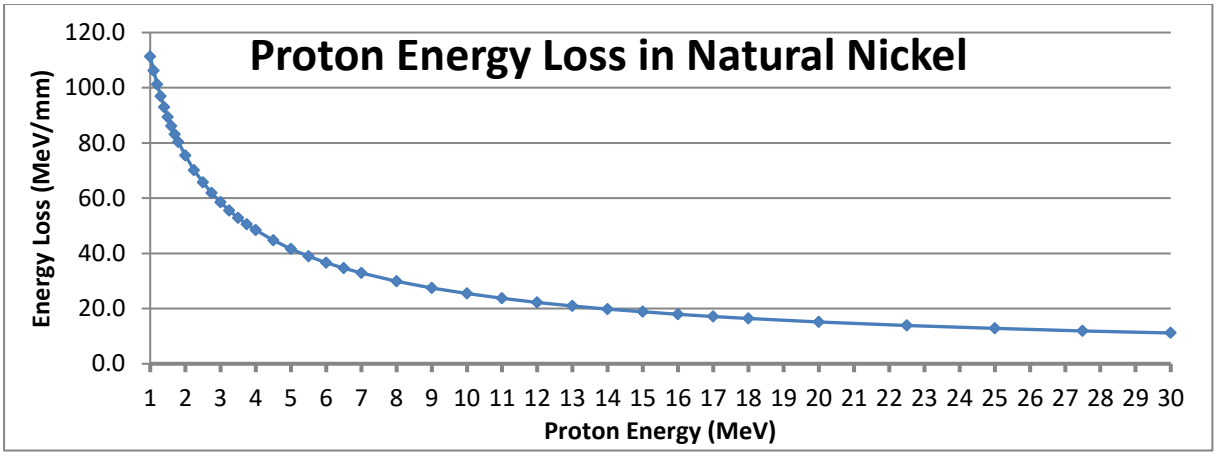


*(Figure 7: Energy Loss of Protons in $^{nat}$Ni Calculated by SRIM).*

When a charged particle travels close enough to interact with a target nucleus, a reaction bringing about a change in the target nuclei mass and/or atomic number may take place if important criteria are met. These criteria can be seen as 'barriers' to a nuclear reaction taking place (Patel, 2011). If the criteria for the reaction are not met, the particle is likely to be scattered by the nucleus changing trajectory and losing energy. This outcome is worthy of note as the particle may go on to a further interaction at a lower energy.

### 1.8 Nuclear Reaction Barriers

In any nuclear reaction the total amount of energy involved must be conserved. This means the rest mass and kinetic energy of the target and projectile must equal the total energy of the reaction products.

This can be simplified as:

(Equation 5):

$$Q = \{(M_X + m_x) - (M_Y + m_y) \times C^2$$

where

$Q$ is the energy absorbed or released in the reaction,
$M_X$ is mass of the target,
$m_x$ is mass of the projectile,
$M_Y$ is the mass of the product,
$m_y$ is the mass of the emitted particle,
$C$ is the speed of light.

This equation gives the change in kinetic energy also known as the Q value. The value dictates whether a reaction will give out energy (exothermic) or require input of energy to take place (endothermic). This will depend on whether the change in kinetic energy or Q value is positive or negative. If the Q value is negative, then this will give rise to a threshold energy below which the reaction cannot take place (Patel, 2011). Mass excess data is used for the projectile and target to calculate the Q value. For the reaction of interest to this work ($Ni^{(58)}(p, 2p)Co^{57}$) the Q value is as follows:

$$= (-60.225 + 7.289) - (14.578 + -59.342)$$

$$= -8.17 \text{ MeV}$$

Therefore this reaction is endothermic and requires an energy input of at least 8.2 MeV to take place. In reality the projectile will need to supply more energy than -Q to the nucleus, as some kinetic energy is given to the compound nucleus.

Before a reaction occurs however a charged particle must first overcome the strong electrostatic repulsion from the target nucleus, an effect known as the Coulomb Barrier. This is a very well defined occurrence whereby the accelerated particle must overcome the electrostatic repulsive force from the target atom (see Figure 8).

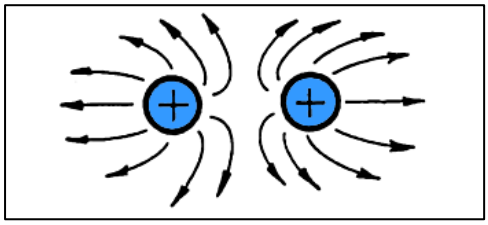

*(Figure 8: Diagram Depicting Electrostatic Repulsion).*

This can be calculated by the equation:
(Equation 6):

$$Ecb \sim \frac{Z_1 Z_2}{(A_1^{1/3} + A_2^{1/3})} \sim \frac{1 \times 28}{1^{1/3} + 58^{1/3}} \text{MeV}$$

where

*Ecb* is the electrostatic force of repulsion in the centre-of-mass-frame,

*Z* is the proton number,

*A* is the nucleon number.

For protons accelerated towards $^{nat}$Ni this equates to roughly 5.7 MeV. Quantum tunnelling effects are not considered.

In general, the threshold for the reaction to occur is set by whichever barrier is higher. In the case of this reaction this threshold is determined by the Q-value and is approximately 8.3 MeV.

### 1.9 Types of Nuclear Reactions

When the necessary criteria have been met for a reaction to take place there are two common outcomes. The first to be considered is a compound nucleus. When an incident proton or charged particle strikes the nucleus of an atom it forms a compound nucleus with that target atom. When this occurs there may be a surplus of kinetic energy that will be distributed between nucleons. The excited compound atom will then undergo nuclear decay and eject a nucleon. A number of high atomic-number radionuclides are produced in this way (Dyson, 1993). This possibility is illustrated by Figure 9.

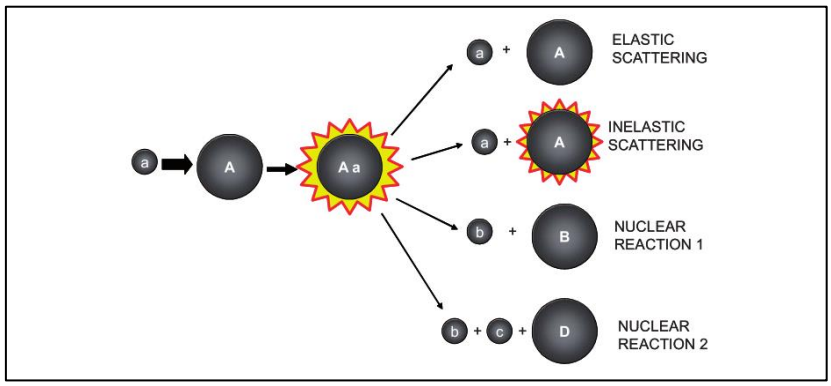


*(Figure 9: Examples of Compound Nucleus Formation and Possible Exit Channels (IAEA, Cyclotron Produced Radionuclides: Principles and Practice (Report 465), 2008)).*

The alternative to compound nucleus formation is a direct reaction mechanism, whereby the incident proton knocks out nucleons in a single step process, directly forming the products (Dyson, 1993).

### 1.10 Nuclear Reaction Cross Section Data

When a charged particle passes through a target there is a chance that a nuclear reaction will occur between the particle and a nucleus. The probability of a reaction taking place is represented by a quantity called the cross-section. One way of visualising this is in terms of two spheres approaching one another, one representing the projectile and one representing the target nucleus. It can be said that if the spheres touch there will be a reaction. The probability of a reaction taking place is represented by the total cross sectional area of the touching spheres. Then the nuclear reaction cross section is given by:

(Equation 7):

$$\sigma_R = \pi r_0^2 (A_p^{1/3} + A_T^{1/3})^2$$

where $r_0$= 1.6 fm

The nuclear reaction cross section can be described in units of barn, where 1b= $10^{-24}$cm$^2$. This nuclear reaction cross section is also a function of energy, which dominates the reaction probability. The unit's name is drawn from the difference in size between the neutron and the nucleus, when compared to a neutron the nucleus appears to be as large as a barn (IAEA, 2009).

The cross section for a particular reaction is best obtained from literature as measurement by theoretical calculation is less accurate. Cross section data for this project will be taken from the EXFOR database maintained by the International Atomic Energy Agency. This resource compiles results from 22,000 experiments performed internationally (Otuka, Dupont, and Semkova, 2014).

## Chapter 2: Theory of Simultaneous Dual Isotope Production

As discussed in Chapter 1, $^{81m}$Kr is an important isotope in nuclear medicine as it allows for the acquisition of images representing the ventilation of patients' lungs. However, these images would be invalidated if the correct quality control of the imaging system had not been performed prior to the patient scan. As Chapter 1 also explains this is best performed with a uniform $^{57}$Co flood source to 'flood' the detector with a uniform field of radiation. This test ensures that the detector responds in a uniform way to radiation.

Production of these isotopes typically takes hours of cyclotron irradiation and a great deal of supporting infrastructure. Commercial facilities will have a vested interest in reducing financial costs associated with isotope production. Academic institutions will equally prize available irradiation time particularly where commercial activities are used to support research applications but place extra time pressures on the machine.

This awareness led to the hypothesis that certain isotope combinations could be produced simultaneously / parasitically where one is produced by using remaining energy from the original reaction.

More specifically whether cyclotron production conditions could be found whereby both $^{81}$Rb and $^{57}$Co yields are acceptable and yet produced simultaneously. Production in this manner would be a novel approach applicable to most facilities operating a cyclotron above 20 MeV and used partly or wholly for isotope production.

Krypton-81m is produced from a $^{81}$Rb / $^{81m}$Kr generator, with the parent $^{81}$Rb being cyclotron produced. The current production method for $^{81}$Rb is proton bombardment of highly enriched $^{82}$Kr gas under several atmospheres of pressure. This allows for the maximisation of $^{82}$Kr (p,2n) $^{81}$Rb reactions. The $^{81}$Rb production at the University of Birmingham follows similar processes as described by the IAEA (IAEA, 2009). A Scanditronix MC40 is used to accelerate protons to 29 MeV which are directed into a $^{82}$Kr gas target (see Figure 10). This target is water cooled to dissipate the thermal energy of the 30 µA proton beam. The target also requires a set of foil 'windows' to allow barometric conditions to transition between high vacuum in the beam line and cyclotron to near 100 psi inside the target. These windows are cooled with helium gas to prevent thermal fatigue and failure.

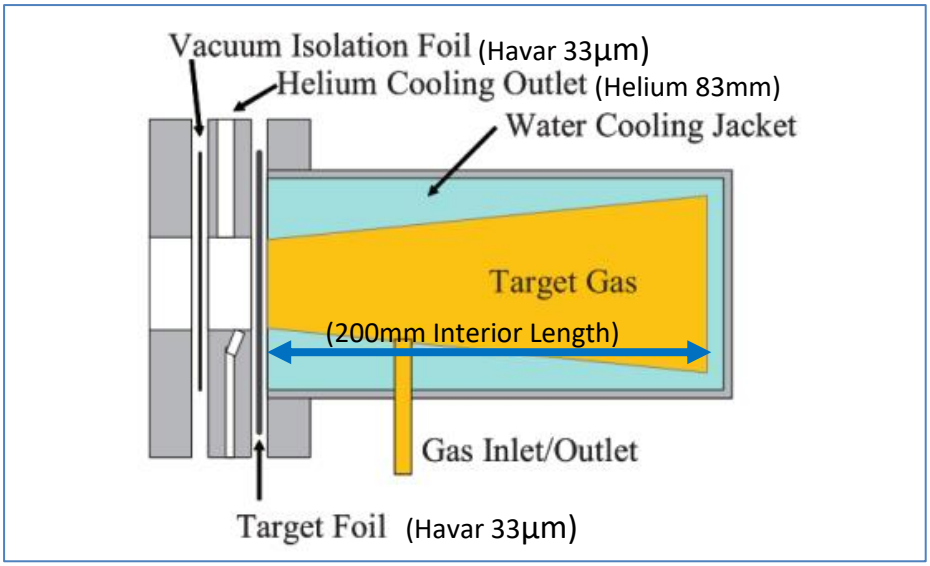


*(Figure 10: Diagram Showing the Internal Specifications of the $^{82}$Kr Gas Target. (Adapted from IAEA, 2009)).*

Upon successfully travelling from the accelerating fields of the cyclotron and entering the gas target, the proton beam can then cause the desired $^{82}$Kr (p,2n) $^{81}$Rb reaction. Immediately after formation, the $^{81}$Rb atom migrates towards the wall of the target as it is much more reactive than the $^{82}$Kr gas. The wall of the aluminium target is electroplated with nickel, this is important for two reasons. Firstly, the nickel coating on the wall of the target allows for the maximum number of rubidium ions to be collected by the potassium chloride (0.001M KCl) wash solution. This target 'wash' dissolves the $^{81}$Rb ions into solution that can be used in the manufacture of the $^{81}$Rb / $^{81m}$Kr gas generator.

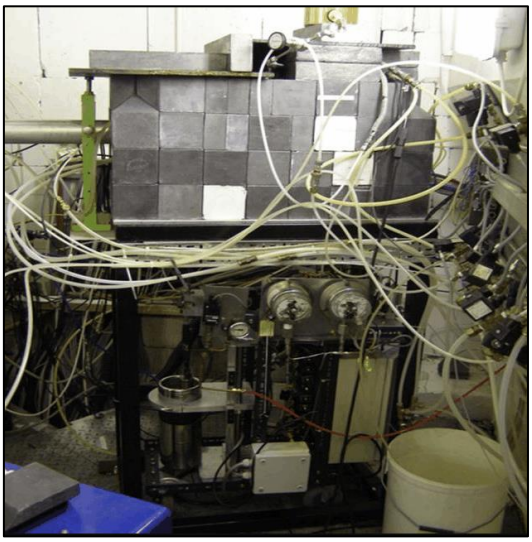

*(Figure 11: Image of the Krypton Gas Target Position at the University of Birmingham).*

Secondly, the $^{nat}$Ni target plating is important because it creates the opportunity for the simultaneous production of $^{57}$Co. If the sole intended product of an irradiation was $^{57}$Co then a number of charged particles could be used. For example, Figure 12 shows three distinct reactions which would yield practical amounts of $^{57}$Co, although others are possible such as:

$^{55}$Mn ($^{3}$He,n) $^{57}$Co,
$^{nat}$Ni($^{3}$He,x) $^{57}$Co,
$^{nat}$Ni(D,x) $^{57}$Co,
$^{nat}$Ni(p,x) $^{57}$Co,
$^{nat}$Fe(p,x) $^{57}$Co,
$^{nat}$Fe(D,x) $^{57}$Co.

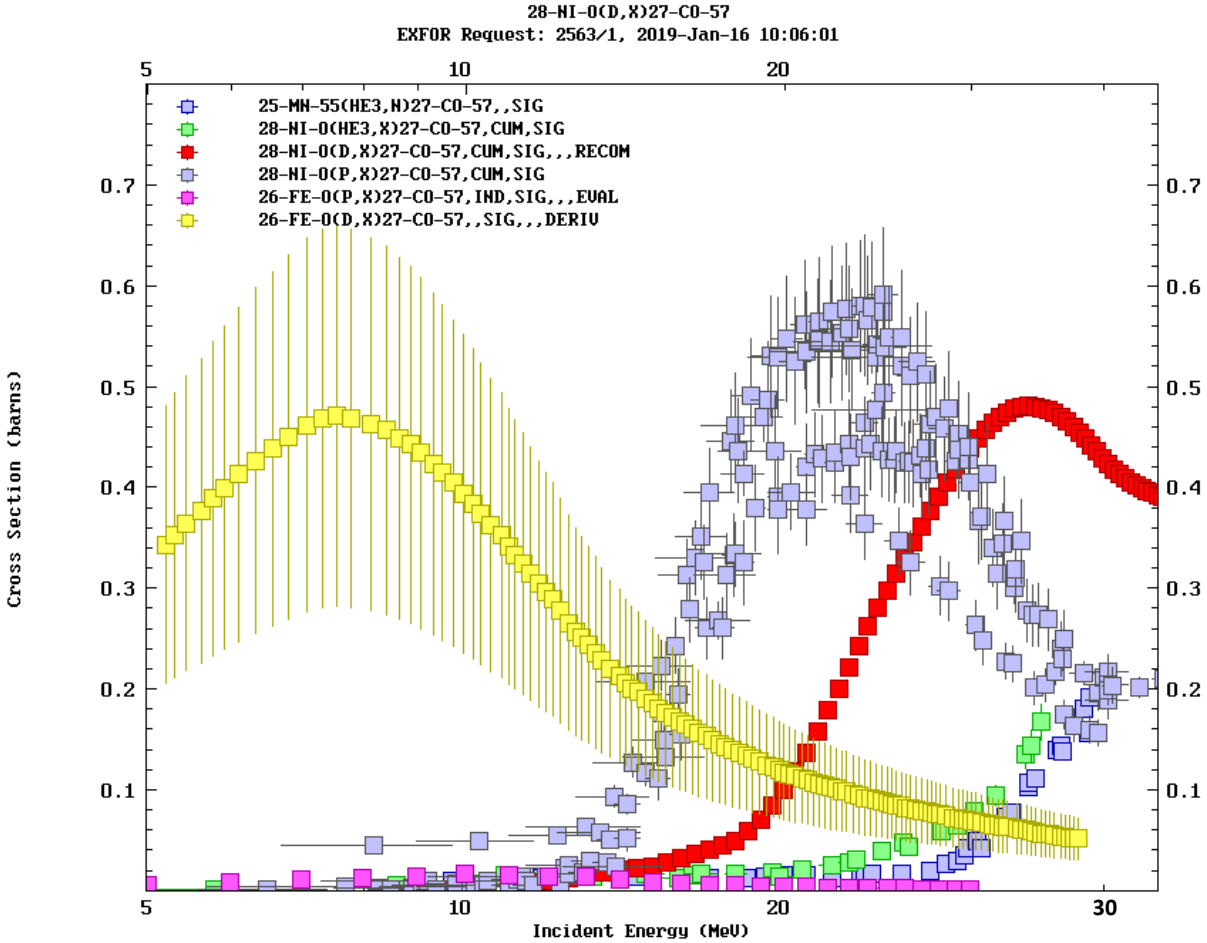


*(Figure 12: Cross Section Data for Reactions Resulting in $^{57}$Co (Otuka, Dupont, and Semkova, 2014)).*

However, as the aim of this work was to simultaneously produce both $^{57}$Co and $^{81}$Rb, reactions involving protons they were therefore, further investigated as proton bombardment is employed in the production of $^{81}$Rb.

This naturally selects (p,x) reactions with nickel because using iron gives very low $^{57}$Co production probability. As shown in the cross section data given in Figure 11, $^{nat}$Ni (p,x) $^{57}$Co shows good chance of achieving practical yields around 20 MeV proton energies. This suggests that conditions can be found allowing efficient co-production of these isotopes; to identify these, more factors needed to be understood regarding both reactions.

### 2.1 Examination of Relevant Proton Kinetics and Reactions

As described the production of $^{81}$Rb is caused by a proton reaction with enriched $^{82}$Kr gas using 29 MeV protons. Reviewing the reported cross section data for $^{nat}$Ni (p,x) $^{57}$Co (see Figure 12) it can be seen that the peak cross section for $^{57}$Co occurs between 20-25 MeV. Natural nickel contains five stable isotopes. When a proton strikes $^{nat}$Ni, a number of isotopes could be created. This is an important consideration given that a $^{57}$Co flood source needs to be at least 99.8% pure.

The next point of investigation was to calculate the energy loss a proton beam would experience after passing through a pressurised $^{82}$Kr gas target. This would give a logical starting point to explore the reactions that may occur when the proton beam reaches the nickel plated rear of the target.

The $^{82}$Kr gas within the target is pressurised to maximise the number of $^{82}$Kr (p,2n) $^{81}$Rb reactions. Before the SRIM program could be used to determine the energy loss, first the density of the $^{82}$Kr gas would have to be calculated at the normal working pressure of 95 psi (81 psig).

Using the ideal gas law:
(Equation 8):

$$PV = nRT$$

$$\rho = \frac{nP}{RT}$$

$$\rho = \frac{(81.913\text{gmol} \times 6.464\text{ATM})}{(0.0831\ \times 293.15\text{K})} \times 10^{-3}$$

$$\rho = 0.022\ \text{g/cm}^3$$

where

*P* is pressure measured in Atmospheres,

*V* is volume,

*n* is grams/mol,

*R* is molar gas constant,

*T* is temperature measured in Kelvin,

*ρ* is density.

The density was then used by the SRIM program to calculate the stopping power of the gas at the working pressure. The calculation was then completed as described above. It was found that a 29 MeV proton would lose 5.8 MeV reducing the energy of the proton to 23.2 MeV. Figure 13 shows a table of nuclides surrounding the target element of interest.

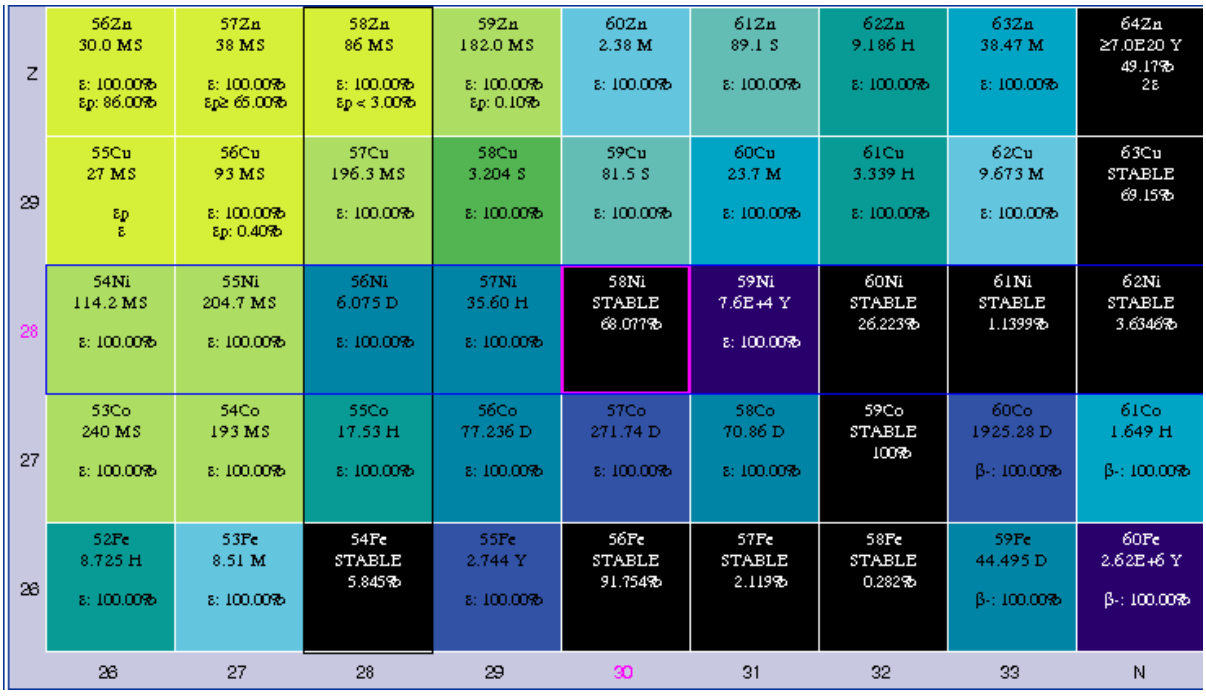


*(Figure 13: Table of Nuclides Showing Relevant Isotopes).*

The cross section data for $^{58}$Ni (p,2p) $^{57}$Co would also need to be known for each calculated energy in each slice. These data were sourced from the EXFOR data base maintained by the IAEA. These data were selected from the advised or recommended cross section. Ideally a spline best fit would give the most accurate result as x (energy) is divided into intervals and polynomial fits applied to each interval independently. The whole fit is then connected. However, due to limitations of available software, polynomial curve fitting of these data was used. The number of

target atoms and beam flux were calculated next. As the target material is non-enriched nickel the number of nuclei is based on the nickel isotopes and their abundances. The main isotopes of nickel are shown in Table 3.

| Isotope of Ni | Relative abundance % |
|---|---|
| **58** | 68.077 |
| **60** | 26.223 |
| **61** | 1.14 |
| **62** | 3.634 |
| **64** | 0.926 |

*(Table 3: Isotopes of Nickel).*

Cross section data were taken from the EXFOR nuclear database maintained by the IAEA. The reaction cross section of $^{nat}$Ni (p,x) $^{57}$Co was selected for analysis. However, there is no IAEA recommended cross section for this reaction. Instead 10 experimental data sets were gathered and plotted for comparison. The average of these datasets was taken and a line of best fit added to the data. The equation for this line of best fit was then used to calculate the cross-section for a given energy (see Figure 14).

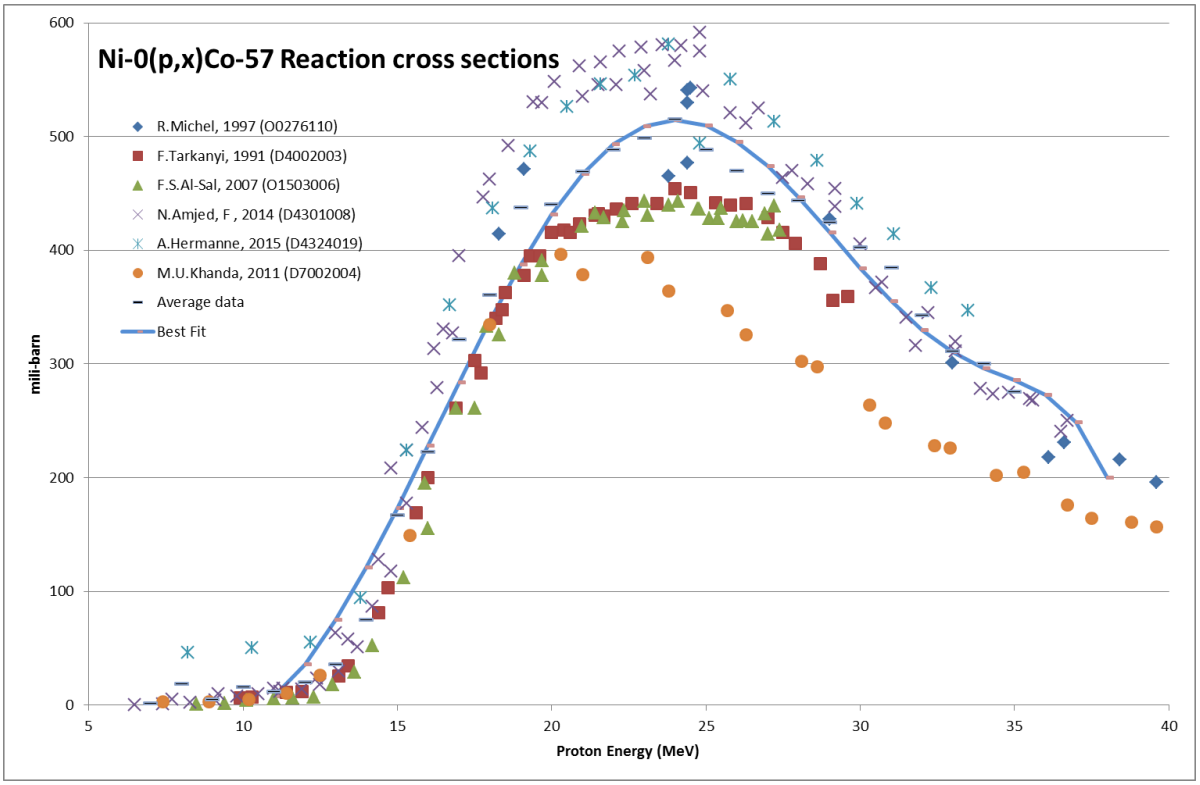


*(Figure 14: Experimental Cross Sections with Average Best Fit).*

Evaluated data were available for specific $^{58}$Ni (p,2p) $^{57}$Co reactions and these data were examined and compared with experimental cross section data. Evaluated

nuclear cross-section data were also available for the other reactions of interest, such as specific contaminating isotopes.

Experimental data for contaminating isotopes arising from the proton bombardment of $^{nat}$Ni were also evaluated. These data were averaged and lines of best fit calculated for each data set, in the same way as the $^{nat}$Ni (p,x) $^{57}$Co reaction (see Figure 15). These complete 'best fit' cross section data were then used in the calculation of the yield for each isotope when bombarding $^{nat}$Ni.

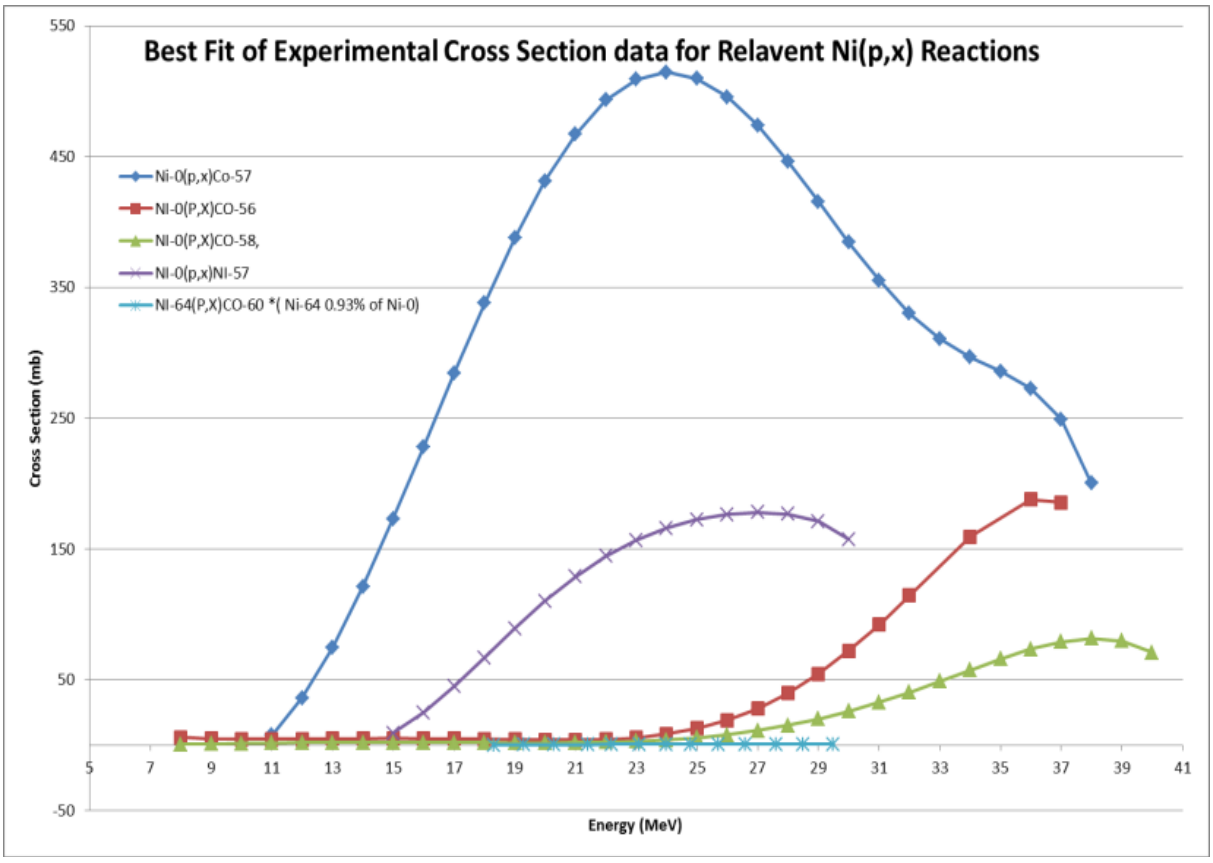


*(Figure 15:Cross Sections of Different Reactions).*

Unfortunately cross sectional data for $^{nat}$Ni (p,x) $^{60}$Co reactions were not available. Instead the specific experimental data for $^{64}$Ni (p,xn) $^{60}$Co were used. As $^{64}$Ni represents 1% of the content of $^{nat}$Ni, 1% of the cross-section value was taken when compared to the other cross sections of natural nickel.

The most effective way to calculate the radioactive yield from a nuclear reaction in a thick target is to electronically compute the necessary factors such as energy loss.

Finally the sum of the cross sections throughout the $^{nat}$Ni slice thickness could be calculated, based on:

(Equation 9):

$$R = n_T I \int_{E_s}^{E_0} \frac{\sigma(E)}{dE/dx} d$$

where

*R* is the number of nuclei formed per second,

$n_T$ is the target thickness in nuclei/cm$^2$,

$I$ is the incident particle number per second and is related to the beam current,

*σ* is the reaction cross-section, or probability of interaction, expressed in cm$^2$ and is a function of energy,

*E* is the energy of the incident particles,

*x* is the distance travelled by the particle,

$\int_{E_s}^{E_0}$ is the integral from the initial energy to the final energy of the incident particle along its path.

From these calculations the radioactive yields and isotopes from the reaction could be predicted:

(Equation 10):

$$Y = n_T I(1 - e^{-\lambda t}) \int_{E_s}^{E_0} \frac{\sigma(E)}{dE/dx} dE$$

A spreadsheet has been devised to perform this function, with each major component of the calculation given a separate tab. The determination of the proton energy loss through the starting material has been calculated using the Stopping Range of Ions in Matter program (SRIM) (Andersen and Ziegler, 1977). This program provided *dE/dx* for a given energy range based on projectile and target material density. An 8$^{th}$ order polynomial fit was applied to these data so that the stopping power could be found for any given energy within the range.

The method employed to integrate the total energy loss through the target was to take the incident proton with energy *E* and calculate the energy loss over a small slice of the target. The final calculated energy of the proton after travelling through the first slice was then used as the initial energy of the proton as it travelled through the next slice. This process was repeated until the proton energy had fallen below the reaction threshold or the sum of the slice thicknesses equalled the total target

thickness. Alternatively the range of the proton was calculated per MeV decreasing in increments of 0.1 MeV; this was then equated to the target thickness.

In thick target studies the energy loss through each material experienced by the proton will be considered, principally this will be: 25 μm of titanium foil used as a window material to separate the vacuum beam line from ambient conditions, and 10mm of air between the target and the exit of the beam line. While the aim of the project was to integrate the nickel disc within the krypton target, initial experiments would be conducted separately using low beam currents on an alternative beam line.

## Chapter 3: Experimental Testing Of Simultaneous Dual Isotope Production

Physical irradiations were planned in order to test the accuracy of the calculations and the ability to predict radioactive yield and isotope composition. The beam characteristics were chosen to produce an amount of radioactivity that would not cause excessive dead time in the gamma camera or cause thermal damage to the target.

Based on the nuclear cross section data it was decided that two irradiations of 29 MeV and 20 MeV would give the most information. This is because 20-29 MeV is the energy range likely to be observed over a 200 mm gas target. The prediction made about the 29 MeV protons is that it would cause $^{nat}$Ni (p,x) $^{56}$Co and $^{nat}$Ni (p,x) $^{58}$Co reactions that are undesirable. Whereas the 20 MeV protons would mainly result in the reaction of interest $^{nat}$Ni (p,x) $^{57}$Co. The resulting yield was calculated for both reactions.

Two $^{nat}$Ni discs of 500 µm thickness were irradiated on separate days by the cyclotron at 29 MeV and 20 MeV respectively. The nickel discs were 25 mm in diameter and housed in a water-cooled jig. Beam current was limited to 400 nA so as to avoid excessive heat and radioactivity within the target. At this beam flux an irradiation time of 30 minutes was sufficient to achieve this. The predicted experimental yield from these irradiation parameters would give enough radioactivity to accurately assess all isotopes that could theoretically be produced from the reaction, yet remain within the gamma camera detector operating range with less than 10% dead time. Excessive radiation flux within a radiation detector can cause an effect known as dead time, whereby the rate of interaction is greater than the rate of detection, thus radiation interactions go un-detected.

The gamma emissions from the irradiated disks were then quantified using a high purity germanium semiconductor detector (HpGe) GEM type manufactured by Ortec instruments and output displayed by Maestro multichannel analyser software. Full specifications are shown in Table 4. The advantage of this type of detector is the excellent energy resolution, as shown by Figure 16.

| Apparatus | Description |
|---|---|
| **Amplifier** | ORTEC Spectroscopy Amplifier, model 5722 |
| **Power Supply** | ORTEC H.V. Power Supply, model 401C |
| **Pre-Amplifier** | ORTEC Pre-amplifier, model GEM-28195 |
| **Detector** | ORTEC HpGe Detector, model SL80190 |

*(Table 4: Specifications of HpGe Detector).*

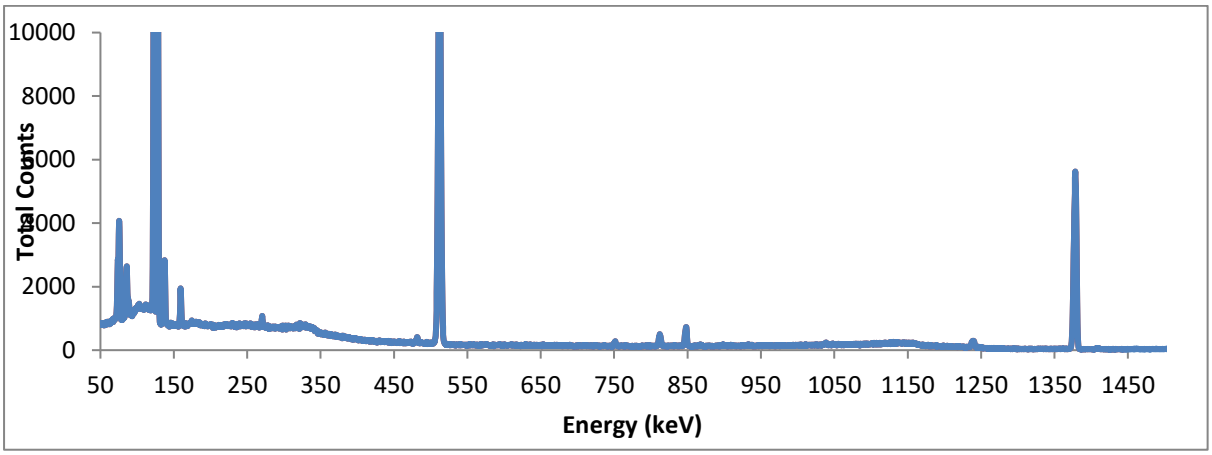


*(Figure 16: Example Spectrum from $^{nat}$Ni Disc Irradiated with 29 MeV Protons, Produced by the HpGe Detector).*

### 3.1 Calibration of High Purity Germanium Detector

A high purity germanium detector was an ideal instrument to use as a gamma ray spectrometer due to the excellent energy resolution of the device. High energy resolution was desirable as the isotopes created during proton bombardment were not always known before acquiring a sample spectrum. Thus, the ability to resolve principle energy emissions to a high degree was advantageous when identifying the isotopes present in a sample. The detector had a typical energy resolution (full width, half maximum) of around 3% compared to that of a sodium iodide detector at 7-9%.

Once isotopes of interest had been identified it was necessary to quantify the activity. This allowed for the yield of each isotope to be compared to the calculated yield. In order to compare the observed target yields to the predictions made by theoretical calculations a detector efficiency curve was derived for the high purity

germanium detector (HpGe). If the detector efficiency is known in terms of count rate per unit of activity then the sample count rate can be converted to an activity. This conversion factor is normally expressed as c.p.s / kBq.

The detection efficiency calibration was done with particular attention to the energies likely to be used and quantified e.g.: 120 keV for $^{57}$Co. Detector efficiency is dependent on a number of factors, and there are two categories; geometric efficiency and intrinsic efficiency. Total detector efficiency is a function of energy, and therefore, depending on the energy, the most likely photon interaction with the detector will change.

This is reflected in the Log (x,y) scale of the efficiency curve, above the energy where photo-electric interactions become less likely, the relationship between energy and efficiency becomes linear. This energy threshold is approximately 200 keV. Below this energy the detection of a photon is more unpredictable due to the varying layers of the detector and absorption of the gamma rays (Sorenson, 2012).

It is possible to interpolate detection efficiency between known energy points, but only for photon energies above 200 keV. This interpolation would not have been suitable to find the detection efficiency for $^{57}$Co as the principal gamma emission is 121 keV. At this energy the photon interaction with the detector will be dominated by the photoelectric effect. Therefore, to quantify the amount of activity of $^{57}$Co in a sample accurately, the detection efficiency would need to be derived specifically for the energy emission of $^{57}$Co.

An ionisation chamber (Capintec CRC-15r) and data logger was used to determine the activity of a standard source of $^{57}$Co, which gave assurance that the reference activity of the source was known to a high degree of accuracy. The reference activity of the standard $^{57}$Co source was 205.646 MBq on 01/05/2010. By using the NPL recommended decay half-life of 271.8 days, which is known to within 0.05 days, the source activity was calculated to be 1.153 MBq at the time of measurement. By using the data logger to record the output from the ionisation chamber every 60 seconds for 24 hours, and then decay correcting those measurements to the time of counting, an activity of 1.134 MBq was calculated. The ionisation chamber derived activity was found to be within 2% of the reference activity supplied with the source. The ionisation chamber has documented traceability to the NPL primary standard. Once the activity of the standard $^{57}$Co reference source was calculated and validated, it was measured on the HpGe detector at the 33 cm sample counting position. The counts per second detected from this source were taken as the detection efficiency

for $^{57}$Co at the 33 cm counting position. A value of 0.964 c.p.s per kBq of activity was found.

The efficiency value found for $^{57}$Co has the limitation that the source geometry of the standard source was a 10 ml resin vial, whereby the samples to be counted were often nickel disc or foil. This introduces a more distributed source of radioactivity within the 10 ml vial compared to a more focal source of activity within the nickel disc or foil. This will have had an effect on the number of photons reaching the detector from each source. The extent of this geometry difference was not investigated or the effects of self-absorption within the $^{nat}$Ni sample. This will form the largest part of the uncertainty in the activity measurement of the $^{57}$Co samples.

### 3.2 Results from Analysis of Irradiated Discs

The results shown in Table 5 are from irradiated target disks that were measured at a height of 33 cm above the HpGe detector. The predicted activity values (see top row of Table 5) are compared to the observed values (see bottom rows of Table 5). Results are shown for both 29 MeV and 20 MeV.

| 29 MeV 25.25 min @0.4 µA | | | | |
|---|---|---|---|---|
| Isotope | $^{57}$Co | $^{56}$Co | $^{58}$Co | $^{60}$Co |
| Half-Life | 271 d | 77.2 d | 70.9 d | 1925.3 d |
| Predicted Activity (kBq) | **220** | 36.7 | 16 | 0.064 |
| Percentage Relative to $^{57}$Co | | **17%** | **7%** | <0.001% |
| Normalised Production (kBq/min) | 8.7 | 1.5 | 0.6 | 0 |
| Observed Activity (kBq) | **205** | 40 | 25 | |
| Percentage Relative to $^{57}$Co | | **20%** | **12%** | |
| 20 MeV 62.5 min @0.4 µA | | | | |
| Isotope | $^{57}$Co | $^{56}$Co | $^{58}$Co | $^{60}$Co |
| Half-Life | 271 d | 77.2 d | 70.9 d | 1925.3 d |
| Predicted Activity (kBq) | **255** | 18 | 8 | 0 |
| Percentage Relative to $^{57}$Co | | **7%** | **3%** | 0% |
| Normalised Production (kBq/min) | 4.1 | 0.3 | 0.1 | 0 |
| Observed activity (kBq) | **231** | 6 | 9 | |
| Percentage Relative to $^{57}$Co | | **3%** | **4%** | |

*(Table 5: Results of $^{nat}$Ni Irradiation (+/- 5% error is assumed)).*

The following spectra (see Figure 17 and 18) show prominent gamma rays at 120 keV in addition to several high energy emissions belonging to contaminant isotopes.

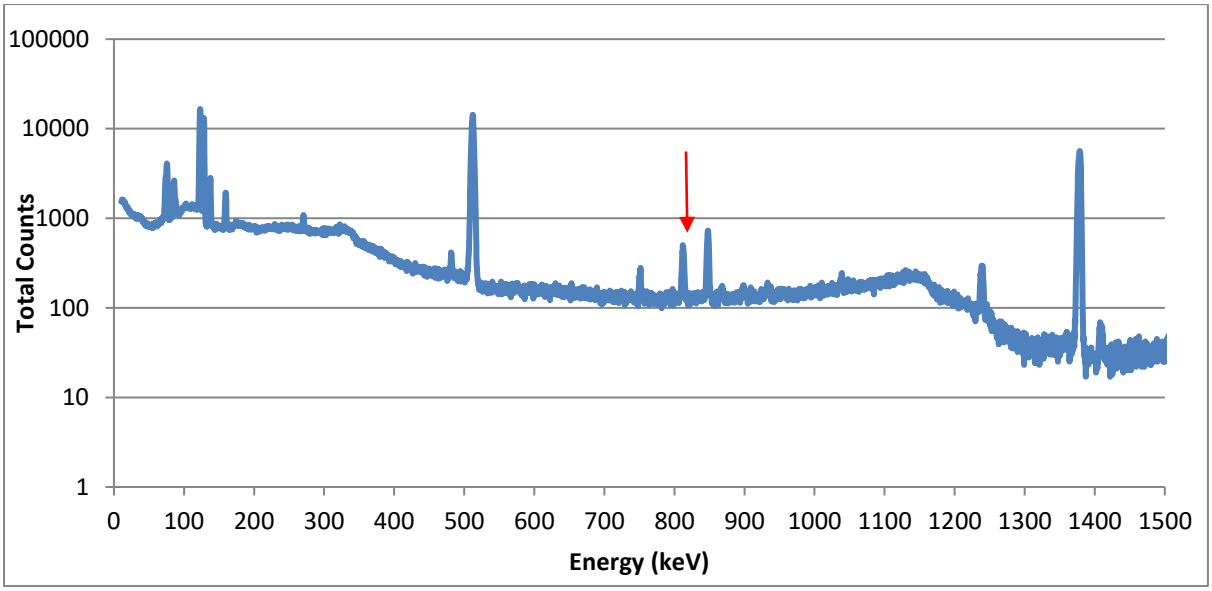


*(Figure 17: Spectrum Acquired 6 Days Post Irradiation of Target $^{nat}$Ni Disc Irradiated with 29 MeV Protons).*

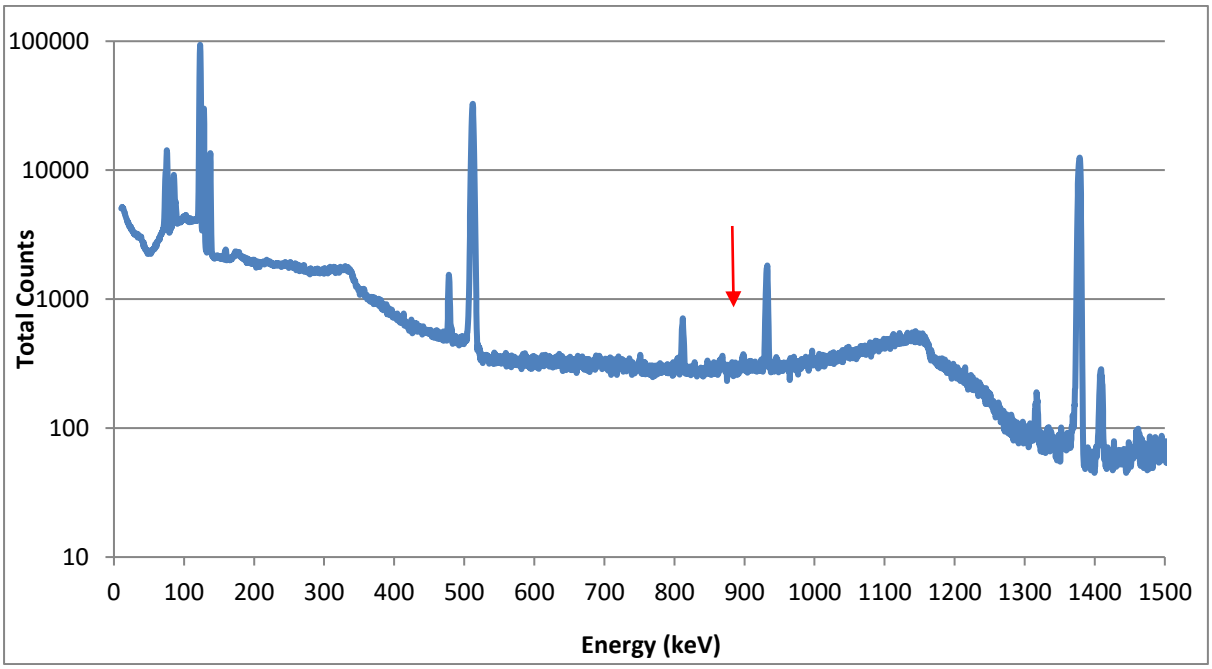


*(Figure 18: Spectrum Acquired 7 Days Post Irradiation of Target $^{nat}$Ni Disc Irradiated with 20 MeV Protons. Red Arrow indicates lack of contaminant peak).*

### 3.3 Discussion of Experimental Results

As shown the experimental results were a good match to the theoretical predictions for $^{57}$Co activities, validating the mathematical model to some degree. The activity values for $^{57}$Co are within 10% of the predicted values. This level of agreement is encouraging given the uncertainty around the averaged cross section and experimental factors such as measurement of beam fluence.

Most importantly the reduction in contaminant isotope activities has been demonstrated experimentally. As seen in Table 5, the $^{56}$Co and $^{58}$Co impurities fall from 20 ± 5% and 12 ± 5% (at 29 MeV) to 3 ± 5% and 4 ± 5% (at 20 MeV) respectively. However, these changes in contaminant isotope activities were not well matched with the predicted values. The predictions significantly underestimate the yield of $^{58}$Co at 29 MeV and overestimate the yield of $^{56}$Co at 20 MeV. The 'normalised' kBq/min values serve to show the drop in total activity yield at the lower 20 MeV energy, which is also in line with calculated reaction rate for this energy.

In so far as the predictions are supported by experiment, it was then possible to make predictions about the optimum target and cyclotron conditions to give the best production results. This represents an early success for the project as the production of $^{57}$Co has been demonstrated with high radionuclide purity. The purity of the $^{57}$Co is important if the nuclide is to be used in any further work.

As the nickel discs were to be inserted into the rear of the krypton target the effects of altering the incident proton beam energy on the $^{81}$Rb production could not go un-assessed. This key area was also tested in a similar way, with two target nickel discs inserted into the back of the $^{82}$Kr gas target. This required the extra calculation of how the proton would lose energy through the pressurised $^{82}$Kr target gas. However the calculations used in this project for the density of the target gas were limited in their accuracy. This is due to the fact that they do not take into account the effects of 'beam heating' within the gas causing localised temperature and therefore density changes (Mulders, 1983). This has the effect of calculating yield results for an ideal target situation, which is an over estimate of what will actually be observed. As shown previously a density change will result in fewer target nuclei that may interact with the proton beam. A 25 MeV proton beam with a current of 30 μA will have a power output of around 0.9 kW causing strong beam heating effects.

### 3.4 Predictions of Optimum Target Thickness and Energy

Once the calculation had been validated the calculator was used to assess how the relevant target yields changed with energy and target thickness. The result of this study are shown in Table 6.

| $^{nat}$Ni (p,x) $^{57}$Co Target Yield Purity | | | | | | | | | | | |
|---|---|---|---|---|---|---|---|---|---|---|---|
| Proton Energy (MeV)➔ | 19 | 20 | 21 | 22 | 23 | 24 | 25 | 26 | 27 | 28 | 29 |
| ↓Target Thickness (cm) 0.1 | 94% | 95% | 96% | 96% | 95% | 93% | 91% | 87% | 81% | 73% | 65% |
| 0.2 | 93% | 94% | 95% | 96% | 96% | 94% | 92% | 89% | 84% | 78% | 70% |
| 0.3 | 92% | 93% | 95% | 95% | 95% | 95% | 94% | 91% | 87% | 81% | 74% |
| 0.4 | 90% | 92% | 94% | 95% | 95% | 95% | 94% | 92% | 89% | 84% | 78% |
| 0.5 | 88% | 91% | 92% | 94% | 95% | 95% | 94% | 93% | 90% | 86% | 81% |
| 0.6 | 86% | 89% | 91% | 93% | 94% | 94% | 94% | 93% | 91% | 88% | 83% |
| 0.7 | 84% | 87% | 90% | 92% | 93% | 94% | 94% | 93% | 91% | 89% | 85% |
| 0.8 | 82% | 85% | 88% | 91% | 92% | 93% | 93% | 93% | 91% | 89% | 86% |
| 0.9 | 82% | 84% | 87% | 89% | 91% | 92% | 93% | 92% | 91% | 89% | 86% |
| 1 | 82% | 84% | 86% | 88% | 90% | 91% | 92% | 92% | 91% | 89% | 87% |

Target purity (Co-57 % of total target activity)

*(Table 6: Table of Target Purity Calculations by Proton Energy and Nickel Disc Thickness).*

Analysis shows that immediately after bombardment of the target $^{57}$Co activity will be a maximum of 96% of the total activity on the target, hence contaminants $^{56}$Co and $^{58}$Co are around 4%. However, at this purity the target yield is only a small percentage of the maximum target yield available. Table 6 shows the relative activities for a given energy and target thickness. The colour in this table now represents the purity of $^{57}$Co and the numerical values give the percentage of the maximum yield.

| $^{nat}$Ni (p,x) $^{57}$Co % of Maximum Target Yield Activity | | | | | | | | | | | |
|---|---|---|---|---|---|---|---|---|---|---|---|
| Proton Energy (MeV)➔ | 19 | 20 | 21 | 22 | 23 | 24 | 25 | 26 | 27 | 28 | 29 |
| ↓Target Thickness (cm) 0.1 | 5% | 5% | 6% | 7% | 6% | 7% | 7% | 7% | 7% | 6% | 6% |
| 0.2 | 11% | 13% | 15% | 17% | 18% | 19% | 19% | 19% | 18% | 18% | 17% |
| 0.3 | 16% | 20% | 23% | 26% | 28% | 30% | 30% | 31% | 30% | 30% | 28% |
| 0.4 | 18% | 23% | 28% | 33% | 37% | 40% | 41% | 42% | 43% | 42% | 41% |
| 0.5 | 18% | 25% | 31% | 37% | 43% | 47% | 51% | 53% | 54% | 54% | 53% |
| 0.6 | 18% | 25% | 32% | 39% | 47% | 53% | 58% | 62% | 65% | 65% | 65% |
| 0.7 | 20% | 25% | 32% | 40% | 48% | 56% | 64% | 69% | 73% | 76% | 76% |
| 0.8 | 30% | 29% | 32% | 40% | 48% | 58% | 66% | 74% | 80% | 84% | 86% |
| 0.9 | 40% | 41% | 39% | 41% | 48% | 57% | 67% | 76% | 84% | 90% | 94% |
| 1 | 40% | 41% | 44% | 49% | 52% | 58% | 67% | 77% | 86% | 94% | 100% |

Target Activity (Activity % of Maximum target activity)

*(Table 7: Table of Percentage of Maximum Target Yields (calculated) by Proton Energy and Nickel Disc Thickness. [Best Efficiency Island Indicated by Blue Oval]).*

It is indicated that a compromise would be needed between the $^{57}$Co yield and purity, which would be found within a "best efficiency island". This island is outlined in Table 7 and possible optimal target thickness and energy would be a $^{nat}$Ni disc of 0.8 mm and incident proton energy of 25 MeV. The oval was selected where isotope

purity did not fall below 94% but target yield remained above 43% as it was predicted that these quantities would not cause dead-time in the gamma camera.

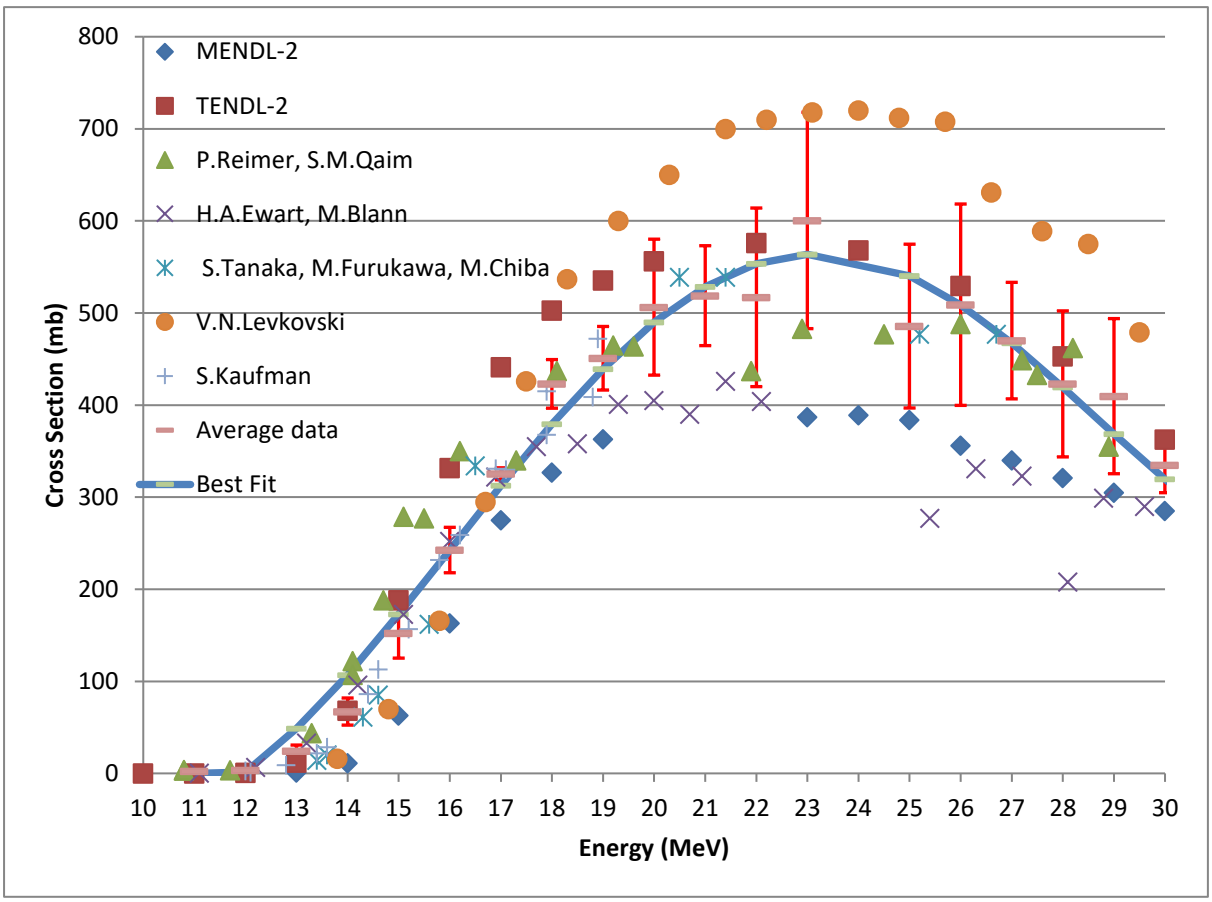


*(Figure 19: Cross Section for Enriched Ni Target Discs $^{58}Ni$ (p,2p) $^{57}Co$).*

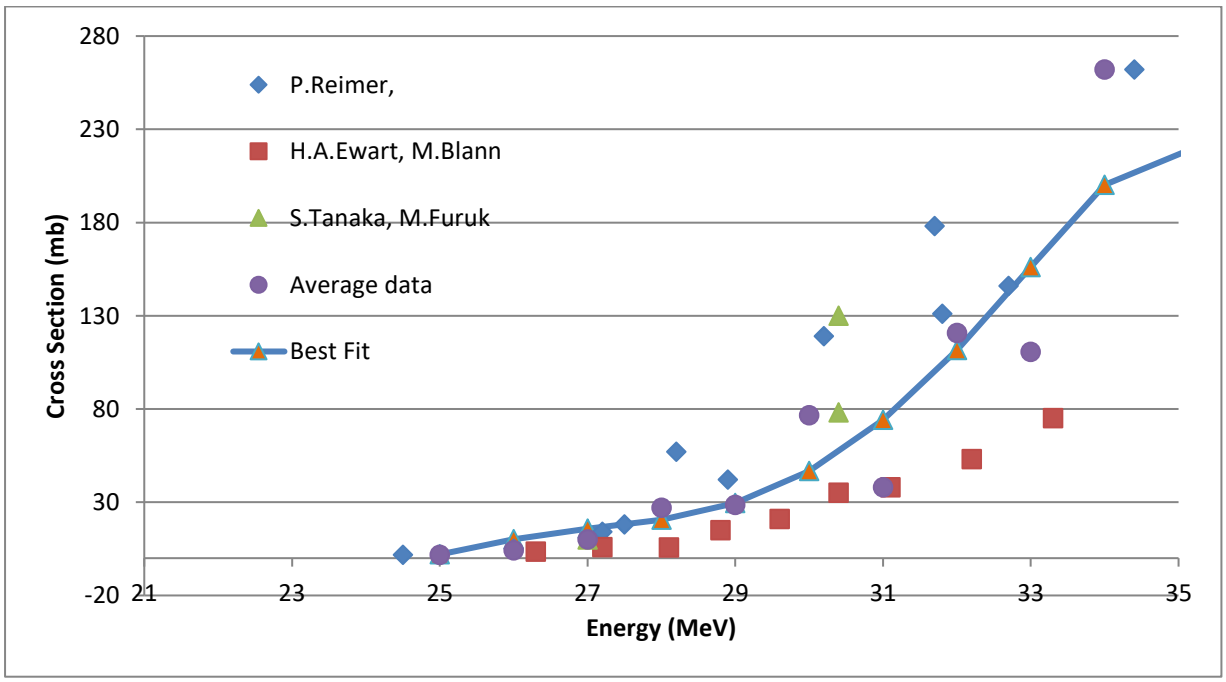


*(Figure 20: Cross Section for Enriched Ni Target Discs $^{58}Ni$ (p,x) $^{56}Co$).*

To examine the theory that purity could change over time, a model of how the relevant isotopes would accumulate over the life span of a rubidium target was calculated. Given the relatively long half-life of $^{57}$Co compared to the contaminant isotopes it is expected that the purity of the $^{57}$Co will rise over time. Table 8 shows the comparison between the activities of 182 simulated successive irradiations 24 hours apart.

| | Relevant Isotope Activities (MBq) | | | | | |
|---|---|---|---|---|---|---|
| | 57Co | 56Co | 58Co | 57Ni | 60Co | 57Co purity % |
| Run 182 | 96.17 | 2.90 | 1.33 | 79.92 | 0.04 | 95.7% |
| After 12 months | 37.81 | 0.11 | 0.04 | 0.00 | 0.04 | 99.5% |

*(Table 8: Predictions of Impurities).*

After 12 months of decay the final purity of the product would reach 99.5% of the total activity. While impressive this purity falls below the purity necessary for use in a final flood source product. A recently supplied commercial flood source was evaluated against the source certificate which quoted all contaminants were less than 0.02%. Spectral analysis and efficiency correction of the spectra from the flood source agreed with this purity value. There are no accepted levels of impurities on the basis that any impurity will cause septal penetration, and therefore the lowest values of impurities are always most desirable.

On realisation that using $^{nat}$Ni target discs would not be able to provide the $^{57}$Co purity necessary for the final intentions of this project, calculations were turned to using highly enriched $^{58}$Ni which has a good cross section as shown in Figure 19. The reason for this is that the (p,2p) reaction can be favoured, therefore minimising any contaminant isotopes. Again the cross sections and purity for energy vs target thickness were considered and Figure 20 shows that $^{56}$Co is not produced in relevant quantities below 25 MeV. By using an enriched Ni disc under the same beam conditions and 182 successive runs, 104 MBq of $^{57}$Co could be produced at 100% purity (if the $^{58}$Ni was enriched to 100% purity) immediately after the final irradiation. This represents a useful gain in activity (+ 65%) and a near perfect radioisotope purity as seen in Table 9.

**$^{58}$Ni (p,2p) $^{57}$Co Target Yield Purity**

| Target Thickness (cm) ↓ / Proton Energy (MeV) → | 19 | 20 | 21 | 22 | 23 | 24 | 25 | 26 | 27 | 28 | 29 |
|---|---|---|---|---|---|---|---|---|---|---|---|
| 0.1 | 100% | 100% | 100% | 100% | 100% | 100% | 100% | 97.2% | 91.5% | 87.6% | 82.1% |
| 0.2 | 100% | 100% | 100% | 100% | 100% | 100% | 100% | 99.0% | 94.8% | 90.1% | 85.4% |
| 0.3 | 100% | 100% | 100% | 100% | 100% | 100% | 100% | 99.4% | 96.9% | 93.0% | 88.0% |
| 0.4 | 100% | 100% | 100% | 100% | 100% | 100% | 100% | 99.6% | 97.8% | 95.0% | 91.1% |
| 0.5 | 100% | 100% | 100% | 100% | 100% | 100% | 100% | 99.6% | 98.3% | 96.2% | 93.1% |
| 0.6 | 100% | 100% | 100% | 100% | 100% | 100% | 100% | 99.7% | 98.5% | 96.8% | 94.4% |
| 0.7 | 100% | 100% | 100% | 100% | 100% | 100% | 100% | 99.7% | 98.7% | 97.3% | 95.3% |
| 0.8 | 100% | 100% | 100% | 100% | 100% | 100% | 100% | 99.7% | 98.8% | 97.6% | 95.8% |
| 0.9 | 100% | 100% | 100% | 100% | 100% | 100% | 100% | 99.8% | 98.9% | 97.7% | 96.2% |
| 1 | 100% | 100% | 100% | 100% | 100% | 100% | 100% | 99.7% | 98.9% | 97.8% | 96.4% |

Target purity (Co-57 % of total target activity)

*(Table 9: Target Purity after Using Enriched $^{58}$Ni).*

# Chapter 4: Further Work to Utilise Simultaneous Dual Isotope Production

## 4.1 Chemical Processing of the Target

The overall aim of the project was to establish a technique of simultaneous isotope production and manufacture of a $^{57}$Co flood source. With this in mind a key part of the method would involve processing the nickel disc into a form that would allow liquid printing. Nitric acid was chosen to dissolve the nickel metal.

A nickel foil was irritated with 20 MeV protons to give an activity of 246 kBq. This foil was then left in a 1M nitric acid solution (20 ml) for approximately 48 hours without any additional heating. On inspection the foil had not noticeably dissolved. The acid was removed and counted on the HpGe detector where it was found that 23% of the $^{57}$Co had been dissolved from the foil. This was an encouraging sign that the chosen acid would be suitable.

The foil was then subject to a 15M nitric acid solution for a 48 hour period. This completely dissolved the nickel foil and remaining $^{57}$Co activity. The acidic solution was then neutralised to avoid potential damage to the inkjet printer.

The chemical reaction for the target material processing is assumed to be:

$Ni + 4HNO_3 \rightarrow Ni(NO_3)_2 + 2\ NO_2 + 2H_2O$.

This is then neutralised with sodium hydroxide to give the following reaction:

$Ni(NO_3)_2 + 2NaOH \rightarrow Ni(OH)_2 + 2NaNO_3$.

The 1M sodium hydroxide solution was added drop wise to the acidic nickel oxide. A pH probe was used to measure the pH of the solution and indicate when pH7 was reached. This process was repeated with a 2.2 g nickel disc containing 2 kBq of $^{57}$Co. It was dissolved according to the chemical process described above. The solution was then neutralised in three separate batches. A sodium hydroxide solution was made using 20 g NaOH dissolved in 200 ml of water. The solution was added drop wise to the nickel nitrate solution until a pH change was seen.

Following the neutralisation each 50 ml batch was then filtered using qualitative filter discs to assess the ion solubility in the solution. Spectral analysis was performed on the sample pre and post neutralisation. An activity loss of not more than 10% was seen indicating that the $^{57}$Co had remained dissolved in the solution.

The next step was to reduce the volume of the 150 ml neutralised $^{57}$Co solution and evaporate this down to a concentrated level. The high specific activity is needed for

adding to the print cartridge with concentrations around 100 MBq per ml. The solution was heated for 45 mins using a hot plate stirrer and evaporated to the point of precipitation. The final volume of the solution was reduced to 20 ml. This would give a theoretical activity of around 70-80 MBq / ml based on $^{nat}$Ni disc activity ~1500 MBq. The activity of the final solution was unable to be accurately measured due to being divided into various fractions. However theoretical calculations support this.

### 4.2 Uniform Flood Source Production via Thermal Drop On Demand Printing

The idea of introducing a radioactive substance into a desktop printer using thermal drop on demand printing has recently been established (van Staden et al, 2007). This type of document printing is well suited to the purpose of this project as printing inks are used in a liquid form. This presents the opportunity to mix a radioactive aqueous solution into the ink. The radioactive ink solution is then deposited on a print media as normal or according to the distribution requested by computer software. A HP desk jet 3630 inkjet printer was been selected for the manufacture of the radioactive flood sources due to its refillable ink cartridge and low cost. In order to calculate the concentration of radioactivity required to give the final activity of the source it was first necessary to determine the average mass of the ink deposited on the paper. Firstly, 3 sheets of 40 gsm plain white office paper were accurately weighed on a balance before a homogenous black square was printed over the entire surface of the paper. The paper was then again weighed on the balance so the average mass of the ink could be determined. The amount of ink found to be dispensed from the ink cartridge was 0.3 g. To produce a flood source of a useful activity it is expected that a specific activity concentration of 100 MBq /ml solution would be needed.

On 05/07/16 $^{99m}$Tc was mixed with refillable ink and added to an empty ink cartridge. Then 1 ml of Pertechnetate ($^{99m}$Tc) was withdrawn into a 5 ml syringe. The radioactivity was first measured in an ionization chamber and then a further 2 ml of refillable black ink was added. The mass of the syringe was then measured on high accuracy lab scales. Then the radioactive ink was inverted several times before being added to the black ink cartridge. The syringe was again measured for radioactivity and weighed so that the exact amount of radioactivity per gram of ink could be calculated. Table 3 in the results appendix shows the activities of the printed pages. Once arbitrary black ink distributions could be uniformly printed, then four separate A4 printed sheets were joined together to form a large A2 size flood source. This arrangement can be seen in Figure 21.


*(Figure 21: Photo Showing Composite Flood Source in Foreground, with Inkjet Printer Behind. Image taken at City Hospital Birmingham, Hot Lab).*

The flood source was then imaged on a GE INFINIA gamma camera using the standard flood source program for a total of 5 million image counts. Then the resulting image was analysed using the standard GE quality control software. The results of this analysis are shown in Figure 22 and Figure 23.

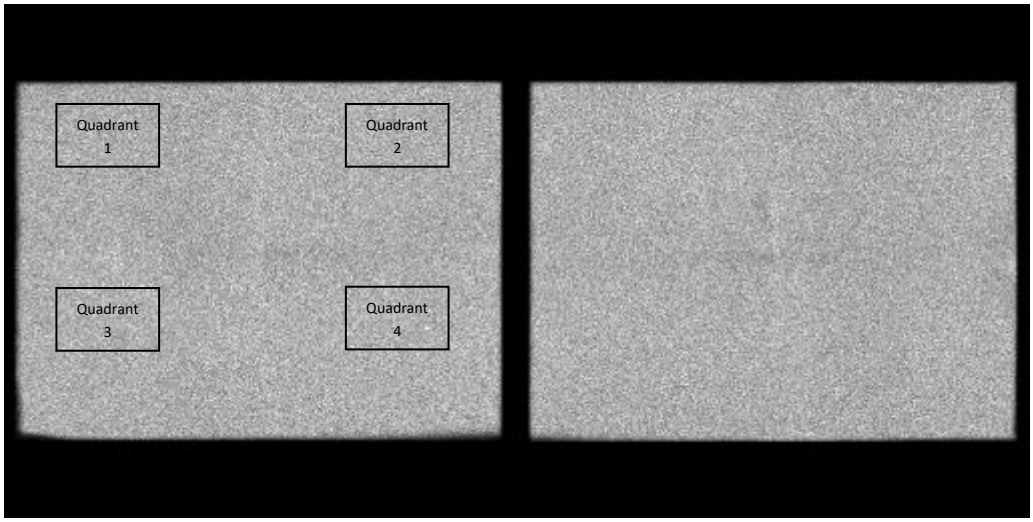


*(Figure 22: 5M Count Flood Source Images: Detector Head 1 Image also Showing A4 Quadrants (left) and Detector Head 2 Image (right). Note: Central Artifacts Caused by Overlapping of Paper Joints).*


*(Figure 23: Output from Standard GE Quality Control Software).*

A further analysis was conducted on the flood source according to NEMA standards. The flood image was also re-windowed to highlight differences in pixel values.

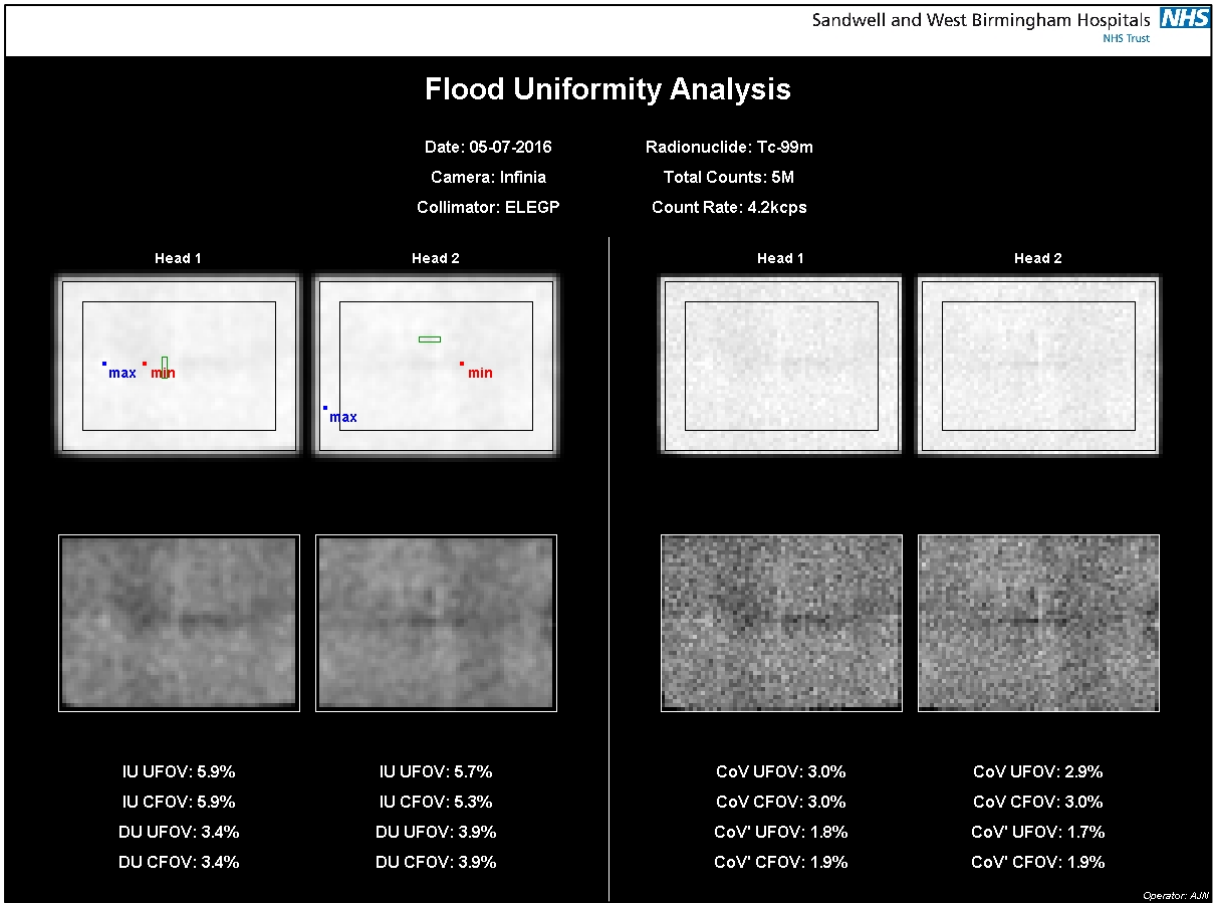


*(Figure 24: NEMA Analysis of 5M Count Composite Flood Image).*

Windowing of the flood image shows some possible areas of non-uniformity within individual printed areas (see Figure 24). Each A4 quadrant was then further analysed to establish maximum printer uniformity. In order to achieve the final objective of this project it would be necessary to demonstrate the concept of adding liquid $^{57}$Co to the ink cartridge of an ink jet printer. Given the long half-life of $^{57}$Co this was not performed at this experimental stage.

# Chapter 5: Discussion of Findings

## 5.1 Evaluating Cross Section Data

A central component of this project was to use and evaluate nuclear cross section data supplied by the International Atomic Energy Agency's EXFOR database. For a number of reactions specific cross sectional data were not available or numerous cross sections have been reported. Using an average of the available cross section data provided a solution to this, which was deemed acceptable as the EXFOR data base for isotope production is still being compiled (Otuka, Dupont, & Semkova, 2014). However, the average data did not represent a 'smooth' curve that would be expected so an 8th order polynomial was fitted as a best fit curve. The average data used to plot this curve were also subject to a significant variation, as shown by the error bars in Figure 25.

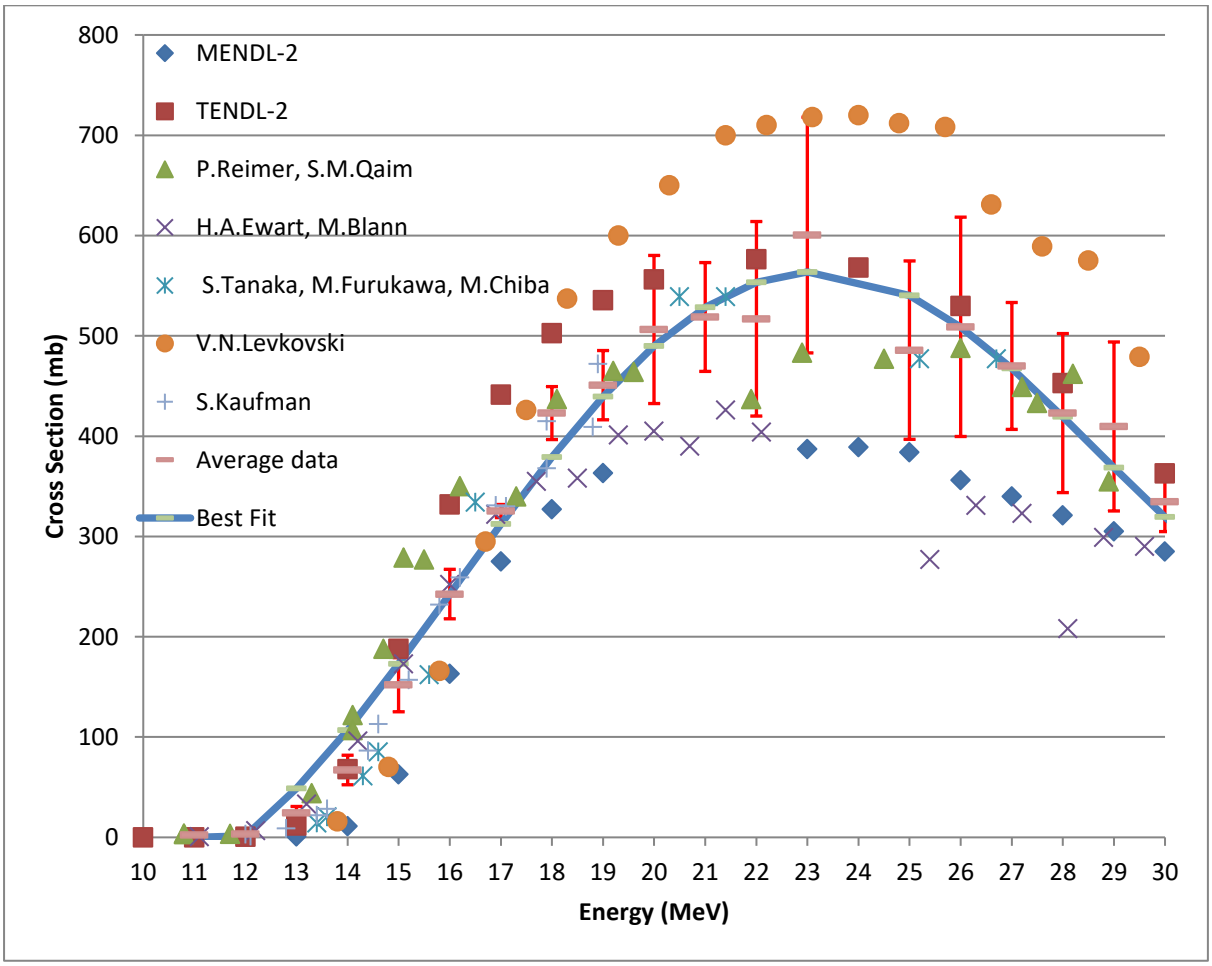


*(Figure 25: Cross Sectional Data Showing Standard Deviation).*

While it was advantageous to use the formula for the 8th order polynomial to interpret the cross section to infinitely small changes in energy between the range,

the certainty at which the cross section for a given energy is known is reduced. The average error of the mean is 15% so this serves as a useful indication of the uncertainty when predicting the yield of $^{57}$Co produced.

### 5.2 Computerized Calculation of Product Yields for Multiple Conditions

The known physical facts and data established in the introductory sections of this work allowed for the generation of a mathematical model for the process at the core of this project. The ability to model nuclear reactions despite some anomalies with accuracy, and calculating production yields has been a key advantage to achieving the desired objectives; namely finding the optimum conditions in which $^{57}$Co and $^{81}$Rb are produced simultaneously.

An explanation of this model is discussed in the 'Computerised Calculation' section of this project, so here it is only noted that creating the optimal production characteristics for a chosen nuclear reaction depends on a number of parameters. It would not have been advisable to employ a trial and error method to find the optimal production characteristics for the following reasons. Causing a nuclear reaction where unknown radionuclides of unknown quantities are produced, could cause a radiation protection issue for the investigators involved with the project. For example an unwanted radionuclide may have a particularly harmful decay mode such as β decay, as these particles have a high linear energy transfer. The half-life of any such radionuclide may be quite long causing storage and disposal problems for the institution. Also any beam time on an efficiently run cyclotron will always need to be prioritised and consideration given to the cost of any operation.

With this in mind the mathematical model was used to make predictions about the products and quantities resulting from a nuclear reaction between protons and the nickel target material. It was clear that these predictions should be tested under experimental conditions, whereby the products were created in the minimum quantities that allowed for analysis. By examining various theoretical outcomes of the nuclear reaction it was observed that lower incident proton energy would give similar target isotope yields, but with less unwanted or contaminating isotopes. Figure 26 shows the nuclear cross section for $^{57}$Co and unwanted Cobalt isotopes.

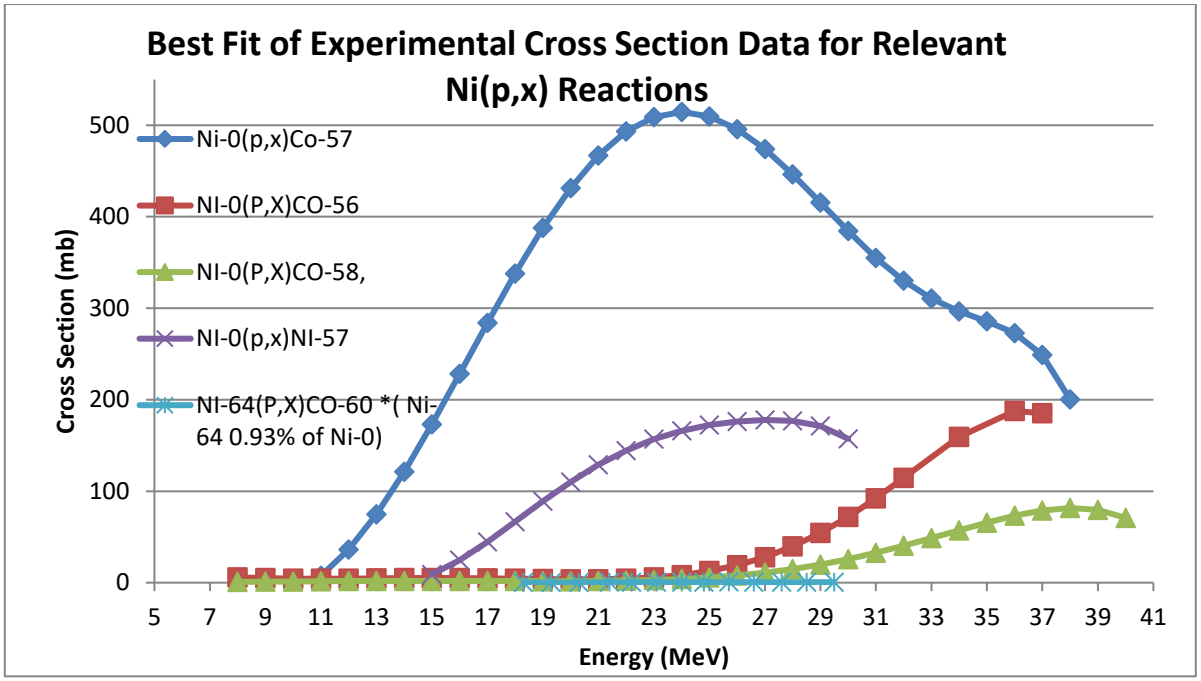


*(Figure 26: Best Fit of Experimental Cross Section Data for Relevant Ni (p,x) Reactions).*

### 5.3 Discussion of Experimental Results

The experimental results shown in Chapter 3 (Table 5 is repeated for ease of reference) were within 10% of predicted activity values for $^{57}$Co, which was encouraging, yet in both irradiations lower than expected $^{57}$Co activities were seen. This could possibly be explained by inaccuracies in the charge collection on the target assembly. The target was not enclosed in a Faraday cage, therefore the integrated charge could have been altered by free ions and delta electrons within the vicinity of the target. Given that both irradiations gave lower than expected results, it is likely that a small proportion of the proton beam was prevented from interacting with the $^{nat}$Ni target disc. This could have been because in the theoretical calculations for direct irradiation of the target disc, energy loss in the vacuum windows and associated helium cooling were not considered. A second factor could have been that a proportion of the proton beam underwent angular broadening as a result of interacting with the target window and therefore struck the target housing rather than the $^{nat}$Ni target disc causing an increase in accumulated charge without production of $^{57}$Co atoms. Fluctuations in beam shape or an overlooked source of scatter could also explain this reduction.

| 29 MeV 25.25 min @0.4μA | $^{57}$Co | $^{56}$Co | $^{58}$Co | $^{60}$Co |
|---|---|---|---|---|
| Predicted Activity (kBq) | **220** | 36.7 | 16 | 0.064 |
| Percentage Relative to $^{57}$Co | | **17%** | **7%** | 0.00% |
| Normalised (kBq/min) | 8.7 | 1.5 | 0.6 | 0 |
| Observed Activity (kBq) | **205** | 40 | 25 | |
| Percentage Relative to $^{57}$Co | | **20%** | **12%** | |
| | | | | |
| 20 MeV 62.5 min @0.4μA | $^{57}$Co | $^{56}$Co | $^{58}$Co | $^{60}$Co |
| Predicted Activity (kBq) | **255** | 18 | 8 | 0 |
| Percentage Relative to $^{57}$Co | | **7%** | **3%** | 0.06% |
| Normalised (kBq/min) | 4.1 | 0.3 | 0.1 | 0 |
| Observed activity (kBq) | **231** | 6 | 9 | |
| Percentage Relative to $^{57}$Co | | **3%** | **4%** | |

*(Table 5: Results of $^{nat}$Ni Irradiations).*

Additionally, in both irradiations contaminant isotope activities were not well predicted.

Firstly, the 29 MeV irradiation (see top box in Table 5) shows higher contaminant activities than expected. This observation is of greater significance when coupled with the lower $^{57}$Co activity, causing the all-important radionuclide purity to become worse than predicted. On re-examination of the spectra (see Figure 17 and Figure 18) $^{56}$Ni was identified in the 29 MeV disc spectrum which decays to $^{56}$Co, contributing to these impurities. The spectrum shown in Figure 18 (20 MeV irradiation) does not show gamma emission peaks at 750 keV and 812 keV supporting the idea that $^{56}$Ni is produced in a far less quantity at the lower energy. This is consistent with cross section data and the omission of accounting for the $^{56}$Ni decay chain.

In the lower energy irradiation the $^{56}$Co activity was significantly reduced compared with the predicted value. The $^{58}$Co activity was a good match for the predictions. The reason for the lower $^{56}$Co activity is unclear. A possible explanation is that the 'best fit' cross section described in Section 5.2 was in fact an over estimate of the true reaction probability. At 20 MeV the cross section for the $^{58}$Ni (p,$^{3}$He) $^{56}$Co is likely to be less than 10 mb therefore making quantification of activity more challenging.

### 5.4 Discussion of Live Rubidium / Cobalt Production

Currently routine production of $^{81}$Rb takes place using proton energies of 29 MeV. After examining the above cross section it was clear that protons with an incident energy of 25 MeV on the krypton target gas falling to 20 MeV at the back of the

target would produce a similar $^{57}$Co yield, yet have a much lower contaminant yield. As these two energies were likely to represent the relevant upper and lower range of particle energies they were chosen for experimental testing.

A nickel disc was irradiated under krypton production conditions with an incident proton energy of 27 MeV over a period of 2 months, in conjunction with another project. The beam current was varied during this time. An analysis of the radioactive spectrum revealed that the contaminant isotopes were in keeping with the levels expected from a 27 MeV proton passing through 200 mm of krypton-82 at the calculated density of 0.022 g/cm$^3$.This energy is still within the cross section for the contaminant isotopes of $^{56}$Co and $^{58}$Co. A beam energy of 27 MeV was used instead of 25 MeV as this maintains the required yield of $^{81}$Rb while achieving the purity of $^{57}$Co, therefore it is proposed that the incident proton energy is reduced to 27 MeV which would reduce the energy of the protons interacting with the nickel to around 20 MeV. This would avoid the contaminant cross sections. These estimates have not taken into account the Havar windows and helium cooling gap. There will be some energy lost when proton interacts with these components. The cross section for rubidium would also need further examination to ensure that the rubidium contaminant isotope ratios did not change. This could be examined with a short irradiation of the rubidium target with a removable nickel disc installed at the back of the target.

### 5.5 Predictions about Target Thickness and Composition

Once the capability to accurately predict the target yield had been established this method was used to model a production period, where a krypton target containing a nickel disc was bombarded for a set number of production runs. This was done to assess the effects of the differing half-lives of $^{57}$Co and the contaminants. It was expected that due to the longer half-life of $^{57}$Co (271.8 d vs 77 d for $^{56}$Co), over time the purity of the sample would rise due to the contaminants decaying at a faster rate. When this theory was modelled it showed that by using a $^{nat}$Ni disc and optimum reaction conditions it was not enough to achieve the very high purity required. This led to the remodelling of the reaction using enriched $^{58}$Ni which possesses a much more favourable cross section. This project did not validate the theory that higher $^{57}$Co purity yields could be achieved with enriched $^{58}$Ni. This was primarily due to the procurement of highly enriched nickel and the reasonable assumption that cross section data provided by EXFOR data base would match experimental observations, as had been the case with $^{nat}$Ni experiments.

### 5.6 Production of Radioactive Flood Sources

The work performed with $^{99m}$Tc filled ink cartridges to form a 'composite flood source' demonstrated the feasibility of this technique. It was interesting to see that on the first attempt at producing a composite flood source, the standard uniformity measures of the gamma camera were achieved. The manufacturer-supplied analysis software found the uniformity of the gamma camera (based on imaging of the composite flood source) to be within the 5% tolerance. Detector Head 1 recorded a 3.7% uniformity value and Detector 2 recorded 3.5%. This value is more accurately described as detector 'non-uniformity' as areas of the image with non-uniformity are identified from the percentage difference between the minimum and maximum numbers of pixel counts.

Further testing was performed on the uniformity images with in-house designed analysis software. This uniformity analysis utilised the 'image j' program and tested according to the more stringent NEMA specifications for uniformity. These specifications limit the amount of image filtering and separate uniformity into two measures, integral and differential uniformity. Integral uniformity is defined by the percentage difference between the minimum and maximum pixel values in the whole image or a global measure. However, differential uniformity looks at the image uniformity on a more local level by comparing neighbouring pixel values. When analysed in this way the composite flood source image did not show uniformity (non-uniformity) below 5%, but just above at 5.9% HD 1 and 5.7% HD 2. This could largely be down to the composite nature of the flood source as all 4 adjoining boundaries needed to meet seamlessly. This effect could be overcome if a large A2 size inkjet printer was used to produce the flood source, eliminating the need to join smaller sections.

## Chapter 6: Conclusion

This project has demonstrated the possibility of parasitic isotope production of $^{81}$Rb and $^{57}$Co from the same proton beam. Moreover the concept of using the $^{57}$Co isotope for routine quality control flood sources has been presented.

By studying the target and product cross sections along with a model of a target life cycle, it has been possible to determine that isotopically enriched $^{58}$Ni would be required. It had been hoped initially to use $^{nat}$Ni target discs inserted into the $^{82}$Kr gas target, however, the resulting purity of $^{57}$Co was less than the current available flood sources. It should be noted that while the purity of the $^{57}$Co from $^{nat}$Ni was less than the existing bench mark, it was still 99.5%.These conclusions were arrived upon after theoretical calculations were performed and validated with practical experiments.

The effect of these impurities is to degrade the image uniformity which the flood source is intended to assess. This is caused by the high-energy gamma emissions from the contaminant isotopes penetrating the lead septa of the collimator in a non-uniform way. The absolute effects on image uniformity using $^{57}$Co from enriched and non-enriched nickel were not assessed, as currently available $^{57}$Co flood sources were used as a bench mark.

The concept of thermal drop on demand printing with $^{99m}$Tc ink solution has been demonstrated as shown by Figure 27 (see Appendix 3). This process could be further developed into a viable production method for $^{57}$Co flood sources by substituting $^{57}$Co for $^{99m}$Tc during experimentation.

It is hoped that the parasitic isotope production concept could be applied to other medically used isotope pairs. This would be an advantageous strategy in the future if more isotope production shifts from neutron activation to proton bombardment by cyclotrons. In theory this would increase the capacity of a medical cyclotron and reduce the time to return on investment.

## Works Cited:

Balashov, V. (1996). *Interaction of Particles and Radiation with Matter.* Springer.

Brookhaven-National-Laboratory. (2016). *NuDat*. Retrieved Sept 26/09/16, 2016, from http://www.nndc.bnl.gov/nudat2/chartNuc.jsp

Dyson, N. (1993). *Radiation Physics with Applications in Medicine and Biology.* Ellis Horwood .

Andersen, H. and Ziegler, J. F., (1977). *Hydrogen Stopping Powers and Ranges in All Elements,vol. 3 of series "Stopping and Ranges of Ions in Matter,".* Pergamon Press, New York.

Heikkinen, P. (1992, 1 1). *CYCLOTRONS .* Retrieved 09 5, 2017, from http://www.iaea.org/inis/collection/NCLCollectionStore/_Public/26/001/26001561.pdf?r=1

IAEA. (2008). *Cyclotron Produced Radionuclides: Principles and Practice (Report 465).* IAEA.

IAEA. (2009). *Cyclotron Produced Radonuclides: Physical Characteristics and Production Methods.* IAEA.

IAEA. (2003). *Manual for reactor produced radioisotopes.* IAEA.

Mulders, J. (n.d.). Yield Curves and Beam Current Dependent Production Rates of Rb Radioisotopes Produced by Protons on a Krypton Gas Target.

Mulders, J. (1983). Yield Curves and Beam Current Dependent Production Rates of Rb Radioisotopes Produced by Protons on a Krypton Gas Target. *International journal of applied radioisotopes, 35* (6), 475 -480.

Nuclear Physics Research Group. (2012). *Positron Imaging Centre*. Retrieved 09 5, 2017, from http://www.np.ph.bham.ac.uk/pic/cyclotron

Otuka, N., Dupont, E., and Semkova, V. (2014). Towards a More Complete and Accurate Experimental Nuclear Reaction Data Library. *Nuclear Data Sheets* , 272-276.

Patel, S. (2011). *Nuclear Physics An Indroduction.* Anshan.

Powsner, R. (2008). *Essential Nuclear Medicine Physics* (2 ed.). Blackwell.

Sorenson, J. and Cherry, S. (2012). *Physics in Nuclear Medicine* ( 4th Edition ed.). Saunders.

Van Staden, J. A., du Raan, H., Lötter, M. G., van Aswegen, A., Herbst, C. P. (2007). Production of radioactive quality assurance phantoms using a standard inkjet printer. *PHYSICS IN MEDICINE AND BIOLOGY* , N329-N337.

Webb, S. (1988). *The Physics of Medical Imaging* (1st ed.). Bristol: IOP Publishing Ltd.

Wille, K. (2000). *The Physics of Particle Accelerators- An introduction.* Oxford.

## Appendix 1: Calculations of Radioactive Yield

The radioactive production rate is given by:

$$R = n_T I \int_{E_S}^{E_0} \frac{\sigma(E)}{dE/dx} dE,$$

Where,

*R*= the number of nuclei formed per second,

$N_T$= the target thickness in nuclei /cm$^2$,

$I$= incident particle flux,

$\sigma$= Reaction cross section/ cm$^2$,

*E*= Energy of the incident particles,

*x*= the distance travelled by the particle,

$\int_{E_S}^{E_0}$ =Integral between the incident particle energy and the final energy of the incident particle along it path.

Target thickness in nuclei/cm$^2$

$$n_T = \frac{\rho x}{A_T} N_A .$$

For a compound,

$$N_G = \frac{F_A C N_A}{A_A} .$$

Beam flux or incident particle flux per second,

$$\phi = \frac{I}{eA},$$

$$\phi = \frac{35\ \mu A \times 10^{-4}}{(25\ \text{MeV} \times 10^{8}) \times (10\ \text{mm} \times 10^{-1})} .$$

$$\phi =$$

Target volume,

$$V = l\pi r^2,$$
$$V = 1.1mm \times \pi \times (5)^2,$$
$$V = 0.8718cm^3.$$

Target Density,

$$N_D = \frac{\rho N_A}{A},$$

$$N_D(^{nat}Ni) = \frac{8.908 \times N_A}{(0.68\times0.058)+(0.26\times0.060)},$$
$$N_D(^{nat}Ni) = 9.74650591 \times 10^{25}\text{atoms/cm}^3$$

$$N_D\left(^{58}Ni\right) = 0.68 \times N_D(^{nat}Ni),$$

$$N_D\left(^{58}Ni\right) = 6.627624019 \times 10^{25},$$

$$N_D\left(^{60}Ni\right) = 0.26 \times N_D(^{nat}Ni),$$

$$N_D\left(^{60}Ni\right) = 2.534091537 \times 10^{25}.$$

Number of nuclei,

$$Y = n_T I(1 - e^{-\lambda t}) \int_{E_s}^{E_0} \frac{\sigma(E)}{dE/dx} dE.$$

## Appendix 2: Printed Flood Source Data

The following data were obtained while calculating the total mass of ink held within the ink cartridge and the average mass of ink deposited on the entire paper surface. This was achieved by weighing the ink cartridge when both full and empty, and similarly measuring the activity.

| | | | Mass of radioactive ink | |
|---|---|---|---|---|
| Ink Level | MBq | Time | Mass (g) | |
| Full | 37.7 | 10:30 | 7.1267 | |
| Empty | 1.152 | 10:42 | 4.1627 | |
| Net | 35.6902 | | 2.964 | |
| Decay corr. | 2.0098 | | | |
| MBq/g | | | 12.0412431 | 10:30 |

*(Table 6: Measurements of Ink Cartridge).*

| Print No. | | | Decay corrected | |
|---|---|---|---|---|
| Print 1 | 3.57 | 12:50 | 4.7 | 0.388 |
| Print 2 | 2.5 | 12:50 | 3.3 | 0.272 |
| Print 3 | 1.7 | 13:00 | 2.3 | 0.188 |
| Print 4 | 1.3 | 14:00 | 1.9 | 0.162 |
| Print 5 | 1.5 | 14:05 | 2.3 | 0.188 |
| Print 6 | 1.5 | 14:10 | 2.3 | 0.190 |
| Print 7 | 0 | 15:21 | 0.0 | 0.000 |
| Average | | | 2.8 | 0.231 |
| Stdev | | | 1.4 | 0.117 |
| CoVar | | | 1.7 | |

*(Table 7: Measurements of Printed Flood Sources).*

| | Uniformity | COV |
|---|---|---|
| Q1 | 3.42 | 2.85 |
| Q2 | 2.98 | 2.6 |
| Q3 | 3.63 | 2.7 |
| Q4 | 2.91 | 2.45 |
| Average | 3.24 | 2.65 |

*(Table 8: Results of Uniformity Analysis on the Printed Flood Source Showing Good Uniformity (<5%)).*

This experiment was then repeated using higher activity prints and a 30M count acquisition.

| | | | Mass of radioactive ink | | 05/07/2016 |
|---|---|---|---|---|---|
| | MBq | Time | Mass (g) | | |
| Full | 124 | 14:35 | 10.3408 | | |
| Empty | 1.517 | 14:45 | 4.8647 | | |
| Net | 122.4536 | | 5.4761 | | |
| Decay corr. | 1.5464 | | | | |
| MBq/g | | | 22.36146299 | 14:35 | |
| | | | | | |
| | | | Decay corrected | | |
| Print 1 | 8.72 | 15:00 | 9.1 | 0.409 | Print quality on auto |
| Print 2 | 9.06 | 15:03 | 9.6 | 0.428 | |
| Print 3 | 9.31 | 15:06 | 9.9 | 0.442 | |
| Print 4 | 9.04 | 15:11 | 9.7 | 0.433 | |
| Print 5 | 9.09 | 15:15 | 9.8 | 0.439 | |
| Print 6 | 8.56 | 15:20 | 9.3 | 0.417 | |
| Print 7 | 8.23 | 15:21 | 9.0 | 0.402 | |
| Average | | | 9.5 | 0.424 | |
| Stdev | | | 0.3 | 0.015 | |
| CoVar | | | 0.1 | | |

*(Table 9: Measurements of Ink Cartridge and Subsequent Prints of Flood Source).*

## Appendix 3: Composite Flood Source Image

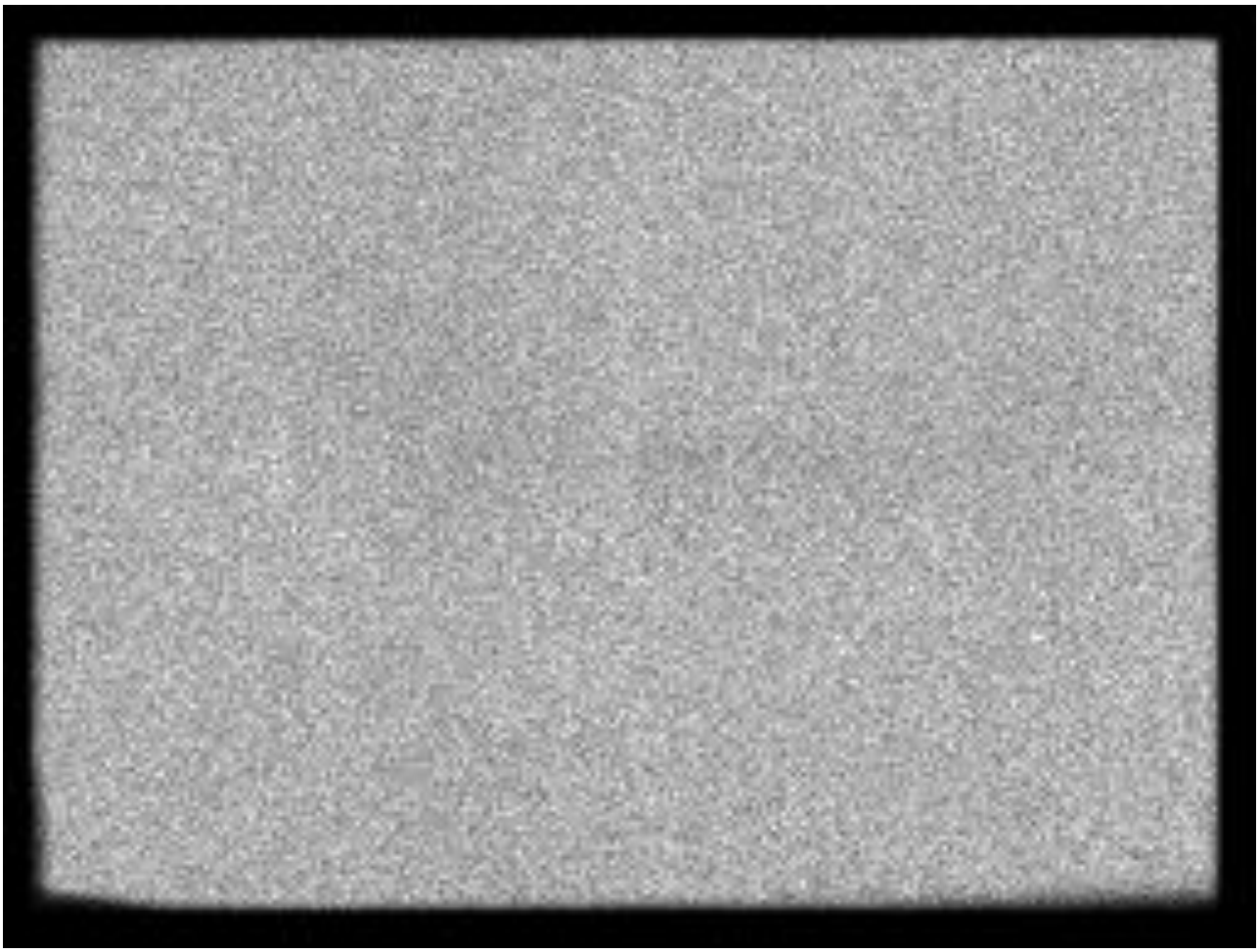

*(Figure 27: 5M Count Image of Printed Flood Source with Uniformity Results Shown in Table 8).*

Figure 27 demonstrates the possibility of manufacturing a flood source via thermal drop on demand printing.